Title: Optimal decision making using grid cells under spatial uncertainty

Authors: Tobias Navarro Schröder[1,2], Benjamin W. Towse[3,4], Neil Burgess[3,4], Caswell Barry[5], Christian F. Doeller[1,2,6]

Affiliation: (1) Kavli Institute for Systems Neuroscience, Centre for Neural Computation, The Egil and Pauline Braathen and Fred Kavli Centre for Cortical Microcircuits, NTNU, Norwegian University of Science and Technology, Trondheim, Norway; (2) Donders Institute for Brain, Cognition and Behaviour, Radboud University, Nijmegen, the Netherlands; (3) UCL Institute of Neurology, (4) UCL Institute of Cognitive Neuroscience; (5) UCL Research Department of Cell and Developmental Biology, University College London, London, UK; (6) St. Olavs Hospital, Trondheim University Hospital, Trondheim, Norway

*Contact Information: t.navarroschroeder@ntnu.no or christian.doeller@ntnu.no

Summary

Minimizing uncertainty in the brain's representation of the environment is essential for accurate decision making but the underlying neural mechanisms remain elusive. Here we show analytically that polarising spatial cues produce an anisotropy in the information available to movement trajectories. Secondly, we simulate a population of entorhinal grid cells in an environment with anisotropic spatial information and show that self-location is decoded with the highest accuracy when grid-patterns are aligned with the axis of greatest information. Thirdly, we expose human participants to a polarised virtual reality (VR) environment and confirm the presence of the predicted asymmetry in spatial navigation performance. Finally, we use fMRI of virtually navigating humans and observe that, as predicted, the orientation of entorhinal grid-like hexa-directional activity is aligned with the environmental axis of greatest spatial information. In sum, we demonstrate a crucial role of the entorhinal grid system in reducing uncertainty in the neural representation of self-location and shed new light on the adaptive spatial computations underlying entorhinal grid representations in the service of optimal decision making and wayfinding.

Keywords: grid cells; computational modeling; decision making; virtual reality; fMRI; spatial navigation.

INTRODUCTION

Knowledge regarding one's environment is inevitably incomplete and often incorrect. The resulting uncertainty constrains the efficacy of behavioural outcomes and, as such, is an important target for optimisation in decision making (Kiani & Shadlen 2009; Daw & Dayan 2014; Pouget et al. 2013; van Bergen et al. 2015; Bach & Dolan 2012; Yoshida & Ishii 2006; Knill & Pouget 2004). Decisions under uncertainty have largely been examined with tasks that focus on relatively isolated aspects of perception. For example, decisions regarding the movement of fields of dots (Kiani & Shadlen 2009), the orientation of gratings (van Bergen et al. 2015), or the sequence of steps leading to a goal (Yoshida & Ishii 2006). Surprisingly, little is known about the role of uncertainty in more ecologically valid situations, such as during free navigation in a spatial memory task. Grid cells are thought to be a key neural system for spatial navigation (Hafting et al. 2005; Burak & Fiete 2009; Bush et al. 2015; McNaughton et al. 2006), in concert with other spatially tuned cell types such as place cells (O'Keefe & Dostrovsky 1971). Here, we bridge this gap by examining the role of a spatial grid code in minimising the impact of uncertainty in the environment in the service of optimising decision making.

Entorhinal grid cells are widely considered to be part of a neural system for self-localisation, deployed in the service of flexible navigation (Hafting et al. 2005; Moser et al. 2014). Their activity patterns tile the environment with approximately equilateral triangles, different modules of grid cells exhibiting different scales of tiling pattern, but broadly similar orientations (Barry, Hayman, Burgess, & Jeffery, 2007; Stensola et al., 2012). The precise mechanisms that control grid firing remain unknown but experimental and computational work suggest that grid-patterns result from the integration of self-motion information stabilised by sensory cues derived from the environment (Burgess et al. 2007; Bush et al. 2014; Burak & Fiete 2009; Giocomo & Hasselmo 2008; McNaughton et al. 2006; Hardcastle et al. 2015). Thus, grid cells maintain their firing patterns in darkness (Hafting et al. 2005) (albeit transiently in mice (Chen et al. 2016)) and are relatively independent of discrete environmental features (Hafting et al. 2005; Moser et al. 2014), ultimately producing patterns that span complex spaces (Carpenter et al. 2015). Nevertheless, grid cell activity is clearly influenced by the sensory environment; contact with a wall is sufficient to reset erroneous firing (Hardcastle et al. 2015) and grid-patterns can be fragmented, polarised or distorted (Derdikman et al. 2009; Stensola et al. 2015; Krupic et al. 2015) by the surrounding cues. Some of these changes result from manipulations made to an existing environment (Barry et al., 2007; Stensola et al., 2012) and are likely transient (Barry et al. 2007; Barry, Ginzberg, et al. 2012). However, in several cases, the observed effects are sustained and appear to originate from an interaction between the grid-pattern and static sensory environment, particular environmental geometry (Krupic et al., 2015; Stensola et al., 2015). For example,

grid-patterns recorded while rats first explore a square enclosure, initially align with an axis parallel to the walls (Stensola et al., 2015) and subsequently rotate to favour a relative angle of roughly 7.5°. Similarly, in a geometrically polarized enclosure, grid firing is strongly distorted, an effect that does not ameliorate with experience (Krupic et al. 2015). Neither of these effects are present in circular environments (Stensola et al. 2015), suggesting that the observed modulation of grid-patterns results from the non-uniformity of spatial cues provided by the enclosure walls. However, it is not known if the polarisation and distortion of the grid is maladaptive – a 'failed' attempt to generate a regular grid which might result in navigational errors (Carpenter & Barry 2016) – or, alternatively, if it confers some advantage. More generally, the systematic changes in grid-patterns following manipulations of an animal's sensory environment promises to provide key insights into the computations that generate grid representations.

Previously, we proposed that grid scale expansion, observed when rodents are placed in an unfamiliar enclosure (Barry, Ginzberg, et al. 2012), is an adaptation to minimise the effect of spatial decoding errors arising due to increased uncertainty in the grid system (Towse et al. 2014). Here, we test if the effect of strongly polarising spatial cues on grid orientation reflects an adaptive change to support spatial navigation. To this end, we employ a combination of biologically inspired simulations, a virtual navigation task, and fMRI-based estimate of entorhinal grid representations (Doeller et al. 2010; Horner et al. 2016; Bellmund et al. 2016; Kunz et al. 2015) referred to as 'hexadirectional activity'. Thereby we aim to shed new light on the spatial computations underlying entorhinal grid representations and their role in processing environmental uncertainty to guide decision making.

RESULTS

Angular change is maximal during movement perpendicular to polarising cues

To investigate the effects of uncertainty on grid cells and decision making, we first determined the presence of anisotropy of spatial information associated with the geometry of a polarised environment. A major source of spatial information during motion is parallax, the apparent change in direction to stationary points in the environment during movement. Below we characterise an anisotropy of such angular change in polarised environments.

Suppose we have a circular arena of radius R centred on the origin, with a polarising cue at distance L (Figure 1A). As an agent moves on a straight path b, we are interested in the angle σ from the agent's heading to the cue, and how it changes when the agent moves. If the cue is within the arena (L<R), then the maximal change in angle (π radians) occurs

when the agent moves towards and through the cue. If the cue is outside the arena (L>R), and the length of the path is very short (i.e. in the limit b → 0) we can calculate the change in angle $\delta\sigma$ to the cue (see Figure 1A, middle panel for example illustration with a longer path):

$$\frac{\delta\sigma}{b} = \frac{\sin\sigma}{a} \tag{1}$$

If the agent is on the x axis (i.e. $y = 0$) then we see that $\delta\sigma$ is proportional to $\sin\sigma$ which is maximal for paths at $\theta = \frac{\pi}{2}$, i.e. movements perpendicular (90°) to the cue.
Hence, spatial information during movement is not isotropic across directions (this conclusion holds on average for the entire arena). Specifically, angular change is maximal during movement perpendicular to polarising cues. Spatial computations, such as Euclidean triangulation, benefit from this parallax information and become more noise resilient (Figure S1-S3).

Impact of environmental geometry on grid pattern may be adaptive

Grid cells might play a role in determining self-location and planning movement trajectories (Bush et al. 2015; Towse et al. 2014; Hafting et al. 2005; Mathis et al. 2012; Burak & Fiete 2009). Biologically plausible simulations of self-localisation with populations of grid cells suggest that, to maintain the most accurate performance possible when spatial uncertainty is greater, the scale of grid cell patterns should expand (Towse et al. 2014) as observed empirically in novel environments (Barry, Ginzberg, et al. 2012). Here, we build on these previously developed models (Mathis et al. 2012; Towse et al. 2014) by inquiring how position decoding using a population of grid cells with coherent orientation is affected by anisotropy in spatial uncertainty (random displacement of grid field). Grid cell ensembles with an axis set at angles from 0 to 30° relative to the axis of greater uncertainty were simulated (due to the six-fold rotational symmetry of the grid pattern, 30° is the largest possible angle between any line and the closest of the pattern's axes). These simulations (see Experimental Procedures) showed that to achieve the most accurate position decoding, grid cells should have one of the three pattern axes oriented at 30° to the axis of least spatial certainty (that is, as far misaligned as possible; Figure 1C, Figure S7-S8). In control experiments, other parameters of the grid cell system were varied and this result remained consistent across these modifications (grid scale, firing rate, number of grid-cell modules; Figure S8). As established above, the axis of lowest spatial certainty corresponds to moving parallel to the polarisation axis defined by the cues. This should lead to a larger impact of noise on spatial computations, as well as to larger observed errors in spatial memory responses.

Effects of anisotropic information on spatial computations and behaviour

Motion induced parallax is a source of navigation-relevant information (Gibson 1958; Raudies & Hasselmo 2015) and lies at the heart of surveying unknown terrain for the creation of spatial maps. Measuring angular changes to landmarks between different observer locations is particularly powerful in combination with distance measurements. For example, this underlies Euclidean triangulation (Crone 1953; United States Department of the Army 1996). Biologically inspired simulations of Euclidean triangulation in polarised environments corroborated that the impact of noise is minimised and that spatial information is maximised for movement perpendicular to the polarisation axis (Figure S1-S3; two-sided Wilcoxon signed-rank test: $Z= 1026.42$, $p<0.001$), results were robust within a plausible range of parameters. To test if the predicted anisotropy in spatial information affect human behaviour, we conducted a behavioural distance estimation task (N=20). After familiarisation with a sparse environment (Figure 2A, Figure S4) polarised by two cues defining an axis, participants navigated to a start location from where they could initiate forward teleportation along one of three directions (-30°, 0° and +30° relative to the polarisation axis; Angles < 90° were chosen to allow testing of many distances with limited field-of-view, see Experimental Procedures; Figure 2B; Figure S4;) and then give an estimate of the traversed distance (Figure 2A, see Experimental Procedures). As predicted, distance estimation was more precise when participants did not move along the polarisation axis, but rather ±30° oblique to it (Figure 2C, $T_{(19)} = 2.7$, $p=0.007$; a similar pattern of results was observed for accuracy, see Figure S5). Hence, spatial navigation performance during more naturalistic free virtual navigation could be expected to also reflect anisotropies in spatial information. We conducted two such VR navigation tasks with concurrent fMRI scanning (N=26 and N=24). Participants freely navigated virtual environments with polarising, extra-maze cues (Figure 3A). In each case they performed a continuous object-location memory task (Doeller et al. 2010; Kunz et al. 2015) with 4 or 6 object-location associations (see Experimental Procedures): navigating to a target location, giving a response, and receiving feedback, interrupted by occasional inter-trial-intervals when a fixation cross was presented on a grey screen for 2 seconds (on average after every third trial; range: 2-4). Object identity and location was randomised across participants (see Experimental Procedures). Despite a relatively sparse environment, participants successfully learnt the object locations (Figure S6). Again, as predicted, participants' spatial responses were more precise (median difference = -4.52% error) perpendicular to the polarisation axis than parallel with it (i.e. X and Y axis, respectively; Figure 3B. One-sided, one-sample T test on pooled data of participant's mean, trial-wise (Y-X)/(X+Y) error. N=50: $T= 2.83$, $p=0.003$). Hence, directions

parallel to the polarisation axis are indeed associated with low spatial certainty. If hexadirectional activity as an index of grid-cell-like representations would exhibit a preferred orientation orthogonal to the polarisation axis, this would provide evidence for an adaptive nature of the impact of environmental geometry on the grid pattern.

Hexadirectional activity clusters orthogonal to polarisation axes

To test environmental anchoring of the entorhinal activity in simple polarised environments, we estimated hexadirectional entorhinal activity (Doeller et al. 2010; Kunz et al. 2015; Horner et al. 2016). In brief, the method takes advantage of a six-fold periodic directional modulation of fMRI activity in entorhinal cortex during virtual movement (see Experimental Procedures). The preferred orientations of hexadirectional entorhinal activity indicated that one of the three putative grid axes clustered approximately perpendicular to an axis defined by the configural cues (Experiment 1, Figure 4) across participants (i.e. the absolute angle to the nearest axis was approximately 30°, corresponding to maximum mis-alignment, Figure 4C-D; N=26, circular V test for deviation from homogeneity perpendicular to the polarisation axis: V=6.68, p=0.032). Note that low-level visual features were equal in all viewing directions. A whole-brain analysis on the remaining half of the data confirmed that activity in right entorhinal cortex was increased for runs at periods of 60° aligned with the optimal orientation (Figure 5A-D, $T_{(25)}$ =4.44, small-volume FWE-corrected p=0.034). In agreement with grid-cell-like representations, runs aligned versus misaligned show largest activity increase for 6-fold (6x) rotational symmetry but not for biologically implausible control models of 5- or 7-fold rotational symmetry (repeated-measures ANOVA: $F(3,25) = 8.3$, $p < 0.001$; Post-hoc, paired t-tests with Holm-Bonferroni correction, * $p<0.05$). No other peaks remained across the cerebrum even at more liberal thresholds ($p<0.001$ uncorrected; $T>3.45$) and neither was there a significant circular clustering of hexadirectional activity in 2 control regions (mammillary bodies, which are close to the hippocampal formation: V test: V=3.33, p=0.822; right, primary visual cortex: V test: V=0.10, p=0.489; See Experimental Procedures).

To test if the environmental anchoring depends on the configural cues, we scanned another group of participants in an environment with a non-configural, polarisation axis consisting of only two extra-maze cues. Estimated hexadirectional activity revealed that one axis clustered again perpendicular to the polarisation axis, replicating the findings from the first experiment (i.e. the absolute angle to the nearest axis was approximately 30°, corresponding to maximum mis-alignment; N=24, circular V test: V = 5.95, p=0.043; Figure 6). Sampling of running directions could not explain these effects in either experiment (Figure S6C-D). In sum, the results from fMRI experiment 1 and the replication in fMRI

experiment 2 provide converging evidence that the preferred hexadirectional entorhinal activity depends on navigation-relevant, polarising cues, independent of the specific type of cue (configural or non-configural). The orthogonal arrangement of hexadirectional activity is in agreement with optimal activity patterns of grid cells for self-localisation, suggesting that the impact of environmental geometry on grid cells is adaptive.

Behavioural anisotropy is linked to hexadirectional orientation

Although there was significantly better spatial memory performance on the X dimension than the Y dimension (see above), this was not equally apparent in all participants (Figure 6D). To take advantage of trial-by-trial variations in spatial memory performance and more directly relate error patterns on the two axes, we computed the anisotropy in spatial memory (Y error – X error) / (Y error + X error) for every trial before averaging. This metric showed a negative correlation with the absolute angle to the nearest axis (Figure 4D, Figure 6C) across participants (Figure 6D; one-sided, Spearman's correlation with pooled data of experiment 1 and experiment 2. N=50: R=0.237, p=0.049). The positive relationship indicates that participants with a more orthogonal orientation of hexadirectional activity were relatively more precise in placing objects on the X dimension than the Y dimension.). This association provides further evidence for an adaptive nature of changes in grid-cell-like representations caused by environmental geometry.

DISCUSSION

To navigate the world around us we often have to make decisions based on noisy and incomplete information. For example, in football a forward player receiving a pass in front of him has to decide to adapt his movement path based on his estimate of angle and speed of the ball. These estimates are imperfect, but can be used to predict the likely point of interception. The neural systems involved in optimal spatial decision making in uncertain situations are likely to involve entorhinal grid cells, given their integration of angular and distance information and their proposed role in self-localisation and navigation (Hafting et al. 2005; Stensola et al. 2012; Bush et al. 2015; Towse et al. 2014). However, the computational mechanisms underlying the grid system remain unknown. Perturbations of the grid pattern in response to environmental geometry (Krupic et al. 2015; Stensola et al. 2015) could be adaptive or rather maladaptive for spatial navigation. Distinguishing between these two options would inform a potential role of grid cells in coping with spatial uncertainty and guiding wayfinding.

To shed light on these issues we combined biologically inspired, computational modelling, behavioural testing, and fMRI. We designed virtual environments (Figure 2-3) where we predicted anisotropies in spatial information across different moving directions (Equation 1 and Figure S1-2). In particular, we focused on the angular change to stationary cues during movement. In line with our predictions, estimation of movement distance was least precise when participants moved along a polarisation axis (Figure 2) and spatial memory performance in two free-navigation, object-location memory tasks was also least precise parallel to a polarisation axis (Figure 3B). To test the theoretical implications of anisotropic spatial information on a system of grid cells, we used biologically inspired simulations. We demonstrate that the most accurate representation of self-location is obtained when grid-patterns are misaligned at 30° with the polarisation axis, reflecting an alignment of the grid pattern with the axis of highest spatial information. fMRI-based estimates of hexadirectional activity in the entorhinal cortex, reflecting putative grid-cell representations (Doeller et al. 2010; Kunz et al. 2015; Bellmund et al. 2016), revealed consistent orientations across participants in two independent experiments (Figure 4 and Figure 6). As predicted, the phase of the hexadirectional signal in entorhinal cortex aligned with the axis of highest spatial information - the optimal grid orientation for decoding self-location. Importantly, the angular offset of hexadirectional activity from the polarisation axis correlated negatively with the anisotropy in spatial memory performance (Figure 6). Taken together, our results provide evidence that the effects of environmental geometry on the grid system are adaptive and angular change to stationary cues play a central role in the computations underlying the grid system. These computations may be sensitive to polarisation axes defined by cues rather than information provided by environmental boundaries per se.

Our findings are in agreement with reports showing that entorhinal fMRI activity correlates with Euclidean distance to a goal location (Howard et al. 2014) and the proposal that grid cells might enable goal-directed vector navigation (Burak & Fiete 2009; Towse et al. 2014; Sreenivasan & Fiete 2011; Stemmler et al. 2015; Mathis et al. 2013; Kubie & Fenton 2012; Erdem & Hasselmo 2013; Bush et al. 2015). Interestingly, both angular and distance information that is needed for triangulation can be derived from either visual or proprioceptive and vestibular cues. For example, visually modulated cells in the rat posterior-parietal cortex signal the egocentric cue direction (Wilber et al. 2014) and head-direction cells in the entorhinal cortex and other regions realign to visible cues, but also function without vision and rely on vestibular information (Taube 2007). On the other hand, distance information can be inferred visually from the relative size of objects and cues (Gibson 1958) or is based on proprioceptive and timing information during movement, both of which modulate grid cell activity (Kraus et al. 2015). Hence, triangulation for wayfinding

could bridge different sensory modalities. Furthermore, it combines egocentric cue directions and distance information to infer map-like, survey representations of the environment, thereby naturally integrating egocentric and allocentric reference frames, which are not mutually exclusive and can work in parallel and across brain regions (Wilber et al. 2014; Epstein 2008; Burgess 2006).

An exciting avenue for future studies is to explicitly examine the effect of anisotropic spatial uncertainty on rodent grid-cell firing. It is known that grid firing exhibits plasticity, regularising and reorienting incrementally with continued experience of an enclosure (Barry et al., 2007; Barry, Heys, & Hasselmo, 2012; Carpenter et al., 2015; Stensola et al., 2015). Our results suggest these changes likely optimise the grid-code, allowing for an increasingly accurate representation of self-location. However, the physiological and circuit mechanisms that facilitate and direct this process are currently unknown. Theoretically, a number of authors have considered the impact of noise in grid cell coding of self-location and its implications for the capacity and error-tolerance of the entorhinal spatial representation (Burak & Fiete 2009; Navratilova et al. 2012; Burgess & Burgess 2014). However, to the best of our knowledge, we have provided the first theoretical and practical account of anisotropic spatial uncertainty on the grid system. It remains to be seen if such asymmetries, which are likely a common feature of the environment (Hardcastle et al. 2015), exert more wide-ranging influences on grid-firing; distorting the grid-pattern or changing the relative scales of different grid modules, for example. In conclusion, our results are consistent with an adaptive and flexible role of grid cells in spatial decision making and wayfinding. This opens up the exciting possibility for a deeper understanding of fundamental neural building blocks of cognition and behaviour.

EXPERIMENTAL PROCEDURES

Simulation of Euclidean triangulation

To test the impact of stochastic fluctuations or noise on triangulation accuracy, we implemented the following simulation in Matlab (2012b, The MathWorks Inc., Massachusetts). Triangles were formed by two points representing start and end points of a straight path in the horizontal plane (e.g. observer locations at time point 0 and time point 1) and one of two polarising, stationary cues. Triangulation was based on the sine rule according to:

$$c = b * sin\,(\sigma) / sin\,(\delta\sigma) \qquad (2)$$

where *c* is the unknown side (distance to the cue at the end point; Figure S1), *b* the known side (distance travelled), σ the angle to the cue at the start point and $\delta\sigma$ the angular change to the cue between start and end point.

Path orientation (azimuth) was varied in steps of 1°, path length remained constant and each path was centred on the origin of the coordinate system. Hence, the start and endpoints of different paths mapped onto a circle. This ensured that the mean distance of different paths to one or multiple cues remained constant. Before the triangulation iterations, random noise was added to the known side and the two distance angles. The error in side length had a mean absolute deviation of roughly 5% the original length (based on typical human distance errors during walking (Elliott 1987)) and was drawn from a Gaussian distribution with mean 0 and a sigma of path length of 15.95. The absolute angular error for a single angle was 5° on average (drawn from a von Mises distribution with mean 0 and a sigma of 6.26) and 15° on average for the absolute cumulative error across all three angles of a triangle. This error rate was based on the mean, absolute angular error observed in humans performing a triangle completion task in virtual reality, which involved pointing to a start location after an outward path with two turns (Wolbers et al. 2007).

Triangulation measurements: noise resilience. Triangulation was repeated for all sides of a triangle using the known base *a*. If the inferred side was the base (the path), triangulation was repeated with both remaining sides serving as the known side and the two results were then averaged. Dual triangulation for the base was done to avoid biased results due to the selection of any one of the remaining sides. Note that the length of the remaining sides was not constant and changed in opposite directions for different path angles, potentially affecting the noise resilience measure at different path angles. This was not a problem in the reverse case, because the base (side *a*) had constant length. The triangulation error for the 3 sides was computed as the absolute difference in the original side length and the length

based on triangulation with noisy input parameters. The 3 error rates were then averaged for further computations and the assessment of noise resilience across paths (Figure S1 – Figure S3). Furthermore, the distance between the most proximal cue to the center of each path (the middle of the base of a triangle) was always equal to the length of the path, with the exception of Figure S3 that shows the effects of different path lengths and different noise levels. In other words, usually the path length was half the length of the polarisation axis. Triangulation to additional cues was performed for a given path angle if these were within ± 90° (determined from the center of a path) to emulate a limited field-of-view. This meant that cues in only that half of the environment were used for triangulation that was faced on a given path (1 point in Figure S1).

Triangulation measurements: triangle quality. The quality measure for triangle shape (triangle area divided by the sum of squares of side lengths; Figure S1 light blue curve) was modified from (Bank & Smith 1997) who describe optimization of finite element triangulations in the generation of meshes.

Computational models of grid cell systems

Model

Self-localisation with a grid cell system under conditions of anisotropic uncertainty was simulated by adapting a previously developed model (Towse et al. 2014), itself based on an earlier model (Mathis et al. 2012), see 'Grid cell system model' below for a complete description. Parameters were as given below except where otherwise specified. The model simulated a population of grid cells organised into four discrete modules with a geometric sequence (scale factor 1.4) of different spatial period sizes and a common orientation. Within each module, 195 grid cells' firing patterns were offset from one another to approximately evenly cover the environment. In each iteration of the model, the true position was specified as the centre of the circular environment. To model anisotropic uncertainty, Gaussian noise was added to the true position, to yield a noisy position estimate. The standard deviation of the noise varied independently in x and y - the environmental axes. All cells within a module received the same noisy position input, but cells in different modules received different input. Each cell was modelled as a Poisson process with maximum firing rate of 10Hz, with its output being the number of spikes generated in a finite read-out period approximating the length of a theta cycle (0.1s).

Assessing decoding quality

For different levels of uncertainty in different directions, we assessed the performance of grid cell systems rotated to set their pattern axes at different orientations relative to the environmental axes in which uncertainty was set. Performance was assessed via an estimate of the maximum-likelihood estimate square error, or MMLE: the mean square difference, across many iterations, between the actual position and the position specified by maximum likelihood decoding of the grid cells' population response. For each combination of levels of uncertainty in x and y, and grid pattern orientation, 75,000 iterations were performed, split between 5 sets in which the square grid across which tuning curves were sampled was rotated. The results of equivalent pairs of uncertainty levels (e.g. standard deviation respectively in x and y of 0 and 5 cm, and 5 and 0 cm) were combined to total 150,000 iterations.

Neuroimaging and behavioural experiments

Participants

FMRI experiment 1. 26 participants took part in the study (12 females, age range: 19–36, mean age: 23 years). Experimental procedures were approved by the local research ethics committee (ethics committee University Duisburg-Essen, Germany and CMO region Arnhem-Nijmegen, NL). Written informed consent was obtained from each participant.

FMRI experiment 2. 25 participants took part in this study (11 females, age range: 18-32, mean age: 24 years). One participant was excluded from the analysis due to poor performance (i.e. 55 trials with no location response within 30 seconds of the respective trial, more than a standard deviation above the mean). Experimental procedures were approved by the local research ethics committee (CMO region Arnhem-Nijmegen, NL). Written informed consent was obtained from each participant.

Behavioural experiment. 20 participants (11 females, age range: 18-24, mean age: 20 years) participated in the behavioural experiment. Experimental procedures were approved by the local research ethics committee (CMO region Arnhem-Nijmegen, NL). Written informed consent was obtained from each participant.

FMRI acquisition*.*

FMRI experiment 1. Blood-oxygenation-level-dependent (BOLD) T2*-weighted functional images were acquired on a 7T Siemens MAGNETOM scanner (Siemens Healthcare, Erlangen, Germany) using a three dimensional echo-planar imaging (3D EPI) pulse sequence (Poser et al. 2010) with a 32-channel surface coil with the following parameters: TR = 2.7 s, TE = 20 ms, flip angle = 14°, voxel size 0.9 × 0.9 × 0.9 mm, field of view (FoV) =

210 mm in each direction, 96 slices, phase encoding acceleration factor = 4, 3D acceleration factor = 2. The scanning session was subdivided into EPI acquisition blocks of 210 volumes each. The majority of participants performed 5 blocks over the course of approximately 55 minutes. Deviations from the 5 blocks in a few participants were due to technical problems or interruptions on behalf of the participants (3 participants had 4 blocks, 2 participants 6 blocks). In addition, T1-weighted structural images (MP2RAGE; voxel size: 0.63 mm isotropic) and a field map (gradient echo; voxel size: 1.8 x 1.8 x 2.2 mm^3) were acquired. Results of an entirely unrelated, task-independent whole-brain connectivity analysis of data from experiment 1 have been described in a previous report (Navarro Schröder et al. 2015).

FMRI experiment 2. BOLD T2*-weighted functional images were acquired on a 3T Siemens Trio scanner (Siemens Healthcare, Erlangen, Germany) using a three dimensional echo-planar imaging (3D EPI) pulse sequence (Poser et al. 2010) with a 32-channel surface coil with the following parameters: TR = 1.8 s, TE = 25 ms, flip angle = 15°, voxel size 2 × 2 × 2 mm, field of view (FoV) = 224 mm in each direction, 64 slices, phase encoding acceleration factor = 2, 3D acceleration factor = 2. Each scanning session consisted of an EPI acquisition block of 1031 volumes on average (range: 661-1200). In addition, T1-weighted structural images (MPRAGE; voxel size, 1 mm isotropic; TR, 2.3 s) and a field map (gradient echo; voxel size, 3.5 x 3.5 x 2 mm^3) were acquired.

Experimental tasks

FMRI experiment 1. Participants freely navigated a 3D virtual reality environment with a modified version of the arena from the studies by Doeller and colleagues (Doeller et al. 2010; Kunz et al. 2015) (Figure 3A) using a 4-button controller. UnrealEngine2 Runtime software (Epic Games) was used to generate the virtual reality task. Instead of two orthogonal axes that are formed by the walls of square enclosures (as in (Krupic et al., 2015; Stensola et al., 2015)) we opted for the simplest case of a single axis, which was determined by extra-maze cues in a circular arena. We hypothesized that the orientation of grid representations would be coherent across participants, as shown in rats moving through square environments, and that this orientation would be determined by the amount of spatial information obtained on movement paths of such orientation. The environment consisted of a circular arena with 12 extra-maze cues, 6 upright and 6 inverted triangles. Two pairs of neighbouring triangles of different orientation comprised the two configural cues on opposite sides of the arena that defined a polarisation axis. To control for possible visual effects on our direction-related analysis, we designed the colour textures for the extra-maze cues in such a way, that the low-level visual features remained equal across cues. Each triangle had a red, green and blue corner, arranged in 1 of 6 possible constellations. The arrangement of

textures was randomised across participants. Participants performed a self-paced object-location memory task that involved collecting and replacing six everyday objects to locations that were randomised across participants. Participants collected each object from its associated location once during an initial phase, by running over it. Navigation was not interrupted during the transitions between trials to enable more natural (ecologically valid) continuous navigation. In each subsequent trial they saw an image (cue) of one of the objects in the upper part of the screen and had to move to the object's associated location and press a button (replace phase). After this response, the object appeared in its associated position and participants collected it again (feedback phase). After an average of 3 trials (range 2-4 trials), a fixation cross on a gray background was presented for 4 seconds (inter-trial-interval, ITI). Object locations were randomised across participants. Since the task was self-paced, the number of trials varied across participants (range: 94-253; mean: 179). Prior to the fMRI experiment, participants performed a similar object-location task with different objects in a different virtual environment outside the scanner to familiarise themselves with the task demands.

FMRI experiment 2. Participants freely navigated the same virtual environment as used in fMRI experiment 1, but with only two extra-maze cues on opposite sides of the arena that defined a polarisation axis (Figure 3A). Participants performed the same object-location memory task described above, except that 4 objects were used instead of 6. Participants performed an average of 117 trials (range: 63-179). Prior to the fMRI experiment, participants performed a similar object-location task with different objects and a different virtual environment outside the scanner to familiarise themselves with the task demands.

Behavioural experiment. Participants freely navigated a virtual reality environment (Figure 2A, Figure S4) by using four buttons on a keyboard to move in the four cardinal directions and the mouse to change horizontal viewing direction. The virtual environment was displayed at 1680x1050 pixel resolution and 60 Hz refresh rate approximately 40cm in front of the participants' eyes. They were teleported between varying start and end locations at one of three possible angles and performed a distance estimation task. The environment was a 'pitch black' space with otherwise only three distinguishable elements. First, it included a background consisting of a white dashed line oriented horizontally and projected at infinity. This background provided minimal visual information to perceive rotational movements as well as motion parallax of a cue viewed from different angles. Second, a cue, consisting of a red circle, was displayed vertically on a fixed location. Third, a red circle indicated the start location of each path with an arrow pointing in the direction of the goal location. The rationale behind using a visually sparse environment and teleportation to the

goal location was to prevent the use of other distance cues, such as cue size (e.g. patches of grass or a boundary) or an estimate of ‘time-of-flight’, respectively. This ensured that the change in size of the cue and the change in angle and motion parallax to the cue from start to the end of a path was the sole means by which the distance estimation task could be performed correctly. Prior to the experiment, participants performed a similar distance estimation task in a different virtual environment to familiarise themselves with the task demands. At the beginning of the behavioural experiment, participants were instructed to approach the cue in order to familiarise themselves with its location and distance.

The trial structure was as follows: Participants were instructed to navigate to the starting point. Once they reached the starting point, their movement was restricted to rotations and the message ‘click right mouse button to teleport ahead’ was displayed (orientation phase one). Participants could self-initiate teleportation to the goal location by a mouse-click and orienting towards the pointing direction of the arrow, at which point the view was frozen and teleportation commenced 2 seconds later. After teleportation to the goal location, the start location became invisible (the red circle with arrow disappeared), movement remained restricted and only rotations were possible and the message ’click right mouse button to give response’ was displayed (orientation phase two). Participants could self-initiate the response phase. Then, a horizontally oriented window was displayed together with the message ‘indicate distance (left = minimum, right = maximum)’ and participants could move the mouse to slide a bar inside the window to indicate how far they thought they were being teleported. The range of possible responses was 0 virtual units (vu) to 6000 vu. For comparison, the arena diameter used in the fMRI studies was 9500 vu for the inner boundary and the length of the polarisation axis (i.e. the distance between opposing, extra-maze cues) was 12064 vu. The range of teleportation distances was 500 vu to 5500 vu (mean = 2742 vu). The response was finalised by another mouse click and subsequently, feedback in the form of smiley faces was given for 2 seconds. The color of a smiley for a response error < 2% of the correct distance was green, light green for an error < 4 %, yellow for an error < 8 %, orange for an error < 16% and red otherwise. During this feedback phase, participants could still move the response bar to see other response-to-feedback mappings (i.e. the smiley associated with a given horizontal pixel location). Once the feedback disappeared, participants were able to freely navigate again. At the beginning of about 50% of trials (determined pseudo-randomly), participants were placed to a point in front of the start location to speed up the experimental procedure (i.e. to reduce navigation time from a goal location to the start location of the subsequent trial) and thereby increase the number of trials. In addition, the orientation phase 1 and 2 were restricted to 6 seconds and the response phase to 4 seconds indicated through the display of a timer. If the time

limit was reached, ‘Time is up! This trial is invalid’ was displayed on a red background and no response was recorded. Teleportation distances and teleportation directions were pseudo-randomly determined on each trial. Teleportation directions were either 0° (approaching the cue on a straight line), -30° or +30°. The location of the cue was at (x = 0 vu , y = 8500 vu) and following the approach of the simulations, all paths were centered on the origin of the coordinate system. However, this would provide a relative advantage to the parallel condition. The size of the cue directly reflects its distance to the observer, which becomes particularly apparent at close proximity. In the -30° and the +30° conditions, the goal location is always further away from the cue compared to the 0° condition at equal teleportation distances. Furthermore, the independent measure (teleportation distance) is linearly associated with goal-to-cue distance only in the 0° condition. To avoid bias due to unequal goal-to-cue distance, we equalized this measure by subtracting the difference across conditions (at equal teleportation distances). In effect, this shifted the teleportation paths in the 0° condition backwards by a given amount (Figure 2B). Due to a limited field-of-view of 85°, testing of large path offsets of e.g. 90° was not feasible. The task duration was limited to 30 minutes in which participants performed an average of 129 self-paced trials (range: 52-238). Prior to the main task, participants performed a training version of the task in a richer virtual environment with a comparable trial structure where the length of the path was not traversed by teleportation but rather through guided movement.

Grid cell system model

Spiking activity of a population of grid cells, organised into 4 (except where otherwise specified) discrete modules by spatial period size, was modelled in a two-dimensional circular environment of radius 50cm using Matlab v.8 (Mathworks). Spatial periods or grid scales, λ_i, were determined as a geometric sequence beginning with λ_1 = 25cm and increasing with a scale factor of 1.4 (except where otherwise specified). Tuning curves for each grid scale λ_i were generated with locations of grid nodes specified as a regular triangular grid and expected firing rate at each location determined by a Gaussian distribution centred on the nearest node:

$$\alpha_{i,j}(x,y) = f_{max} e^{-\frac{d^2}{2\sigma_i^2}}$$

where *j* specifies a particular cell, *d* is the distance from (x,y) to the nearest grid node, f_{max} the maximum firing rate (constant across the population; 10Hz except where otherwise specified), σ_i the tuning width of the grid fields ($\sigma_i = 3\lambda_i/(20\sqrt{\log_e 100})$ following (Mathis et al. 2012).

Within each of the 4 modules, M = 195 offset tuning curves were distributed in a 13 × 15 rectangular grid via translations of this original tuning curve, as well as adding a random translation common to all grids in the module. This resulted in a total of 1560 grid cells in a system. Grid tuning curves could also be rotated to specified orientations; all grid tuning curves always shared a common orientation. All these transformations were performed using cubic interpolation.

In each iteration of the model, the true position (x, y) was specified as the centre of the circular environment (0, 0). To model uncertainty, Gaussian noise, with standard deviation varied independently in x and y, was generated separately for each module and added to (x, y), to yield a noisy position estimate ($x + \varepsilon_{x,i}$, $y + \varepsilon_{y,i}$). Anisotropic uncertainty was produced by independently varying the standard deviations of $\varepsilon_{x,i}$ and $\varepsilon_{y,i}$ between 0 and 5. All cells within a module therefore received the same noisy position input, but cells in different modules received different input. Thus cell firing rate was now modulated according to $\alpha_i (x + \varepsilon_{x,i}, y + \varepsilon_{y,i})$.

The signal extracted from the grid cell system was the number of spikes, *k*, generated by each neuron during a finite read-out period, *T* = 0.1s (the approximate length of a theta cycle) – i.e. a population response $\boldsymbol{K} = (k_1, \ldots, k_N)$. We assume the decoding cannot take the added noise into account in any way, so that given a position *x* the probability of observing the response ***K*** in time T, following (Mathis et al. 2012), is taken to be:

$$P(\boldsymbol{K}|x,y) = \prod Poisson\left(k_{i,j}, T\alpha_{i,j}(x,y)\right) = \prod \frac{\left(T \times \alpha_{i,j}(x,y)\right)^k}{k!} \times e^{-T\alpha_{i,j}(x,y)}$$

where $\alpha_{i,j}(x,y)$ is calculated by cubic interpolation from the tuning curve. From the population response ***K***, we can decode position as the maximum likelihood estimate of *(x, y)*, that is $\hat{x},\hat{y}(\boldsymbol{K})$. Given the initial assumption that all positions within the environment are uniformly likely,

$$\hat{x},\hat{y}(\boldsymbol{K}) = \max P(x,y|\boldsymbol{K}) = \max P(\boldsymbol{K}|x,y)$$

Thus $\hat{x},\hat{y}(\boldsymbol{K})$ may be closely approximated by calculating $P(\boldsymbol{K}|x,y)$ for a sufficiently finely spaced uniform sample of *x* and *y* values across the environment, and selecting the values of x and y which yield the greatest $P(\boldsymbol{K}|x,y)$. We used a spatial bin size of 0.5 cm. Where two or more solutions yielded the same maximal $P(\boldsymbol{K}|x,y)$ (i.e. decoding was ambiguous), one was randomly selected (Mathis et al. 2012; Towse et al. 2014).

Assessing grid system performance

For each combination of levels of uncertainty in x and in y, we assessed the performance of grid systems whose patterns were orientations to these x-y axes from 0° to 30° at intervals of 2.5°. For each case, five experiments each consisting of 15,000 iterations of this procedure were performed. In each of these five experiments, the square grid across which the environment was sampled to produce tuning curves was set at a different orientation to the environment's Cartesian axes, in order to control for any effect of uneven sampling (the orientations were 0° and 4 orientations randomly selected and then used across all conditions). The results of equivalent pairs of uncertainty levels (e.g. standard deviation respectively in x and y of 0 and 5 cm, and 5 and 0 cm) were combined to total 2 × 5 × 75,000 = 150,000 iterations. Using these, accuracy of decoding was assessed via the approximated maximum-likelihood estimate square error, or MMLE, based on the square errors of position decoding:

$$MMLE \approx \frac{1}{75000} \sum_{c=1}^{75000} \left(0 - \hat{x}(\boldsymbol{K}_c)\right)^2 + \left(0 - \hat{y}(\boldsymbol{K}_c)\right)^2$$

FMRI data pre-processing

Image pre-processing and analysis were performed with the Automatic Analysis Toolbox (https://github.com/rhodricusack/automaticanalysis). This involved using custom scripts combined with core functions from FSL 5.0.4 (http://fsl.fmrib.ox.ac.uk/fsl/) and SPM8 (http://www.fil.ion.ucl.ac.uk/spm). SPM was used for an iterative functional image realignment and unwarping procedure to estimate movement parameters (three for rotation, three for translation) and to correct images with respect to gradient-field inhomogeneities caused by motion. To improve co-registration and the creation of a group-specific structural and functional template using the Advanced Neuroimaging Toolbox (ANTS; http://www.picsl.upenn.edu/ANTS/) structural images were de-noised using an optimised non-local means filter (Manjón et al. 2010) and mean EPI images were corrected for gradual changes in signal intensity (bias correction) using SPM. Next, structural images were co-registered (based on mutual information) to the functional images using SPM and brain-extraction was performed using FSL. The resulting skull-stripped structural image was segmented into grey matter (GM), white matter (WM) and cerebro-spinal fluid (CSF) voxel masks. Finally, functional images were spatially smoothed with an isotropic 8-mm full-width-half-maximum Gaussian kernel and high-pass filtering with a 128-s cut-off to reduce low-frequency drift.

Physiological artefact correction.

During the 7T-fMRI acquisition of fMRI experiment 1, we recorded the cardiac pulse signal and respiration of participants by means of an MRI compatible pulse oximeter and pneumatic belt (Siemens Healthcare, Erlangen, Germany) at a sampling rate of 50 Hz. In addition, scanner pulses were recorded in an analogue input for synchronisation of fMRI and physiological data at 200 Hz. Due to technical problems, these data were not available for all scanning blocks and participants (average of 2.7 blocks, range 0 to 5 blocks per participant). Physiological artefact correction was performed for fMRI data with available concurrent physiological data. This involved band-pass filtering the pulse data between 20 and 150 bpm (0.3 and 2.5 Hz, respectively) to improve peak detection. Subsequently, RETROICOR was used to create regressors that were fed into the subject-specific fMRI analyses (GLMs) as confound regressors to remove spurious fluctuations. Fluctuations due to cardiac and respiratory phase were each modeled by 6 regressors for sine and cosine Fourier series components extending to the 3rd harmonic. Two additional regressors modeled lower frequency changes in respiration and heart rate with a sliding window analysis following (Hutton et al. 2011).

Region-of-interest (ROI) definition

Based on our a priori hypothesis (Doeller et al. 2010; Kunz et al. 2015), ROI analyses were performed for the right entorhinal cortex (EC). Right EC ROIs were created on the Montreal Neurological Institute (MNI152) T1 template using a probabilistic atlas based on cytoarchitectonic mapping of ten human post-mortem brains (Amunts et al. 2005) with FSL 5.0.4 (http://fsl.fmrib.ox.ac.uk/fsl/). The probability threshold was conservative (95%) for the estimation of hexadirectional orientations and liberal (0%, i.e. including all voxels with non-zero probability) for the small volume correction of the mask. Thresholded masks were binarised and converted to NiFTI file format and then normalised to the space of the individual functional images via the group-specific EPI template (Figure S9) using the Advanced Neuroimaging Toolbox (ANTS; http://www.picsl.upenn.edu/ANTS/). SPM was used to reslice the ROI mask dimensions to the EPI dimension, which was again followed by binarisation of the masks. Through the same procedure, a right, primary visual cortex (Amunts et al. 2000) mask (95% threshold) and a mamillary body (Bürgel et al. 2006) mask (25% threshold) were created for control analyses.

Analysis of fMRI time series

Following pre-processing, fMRI time series were modeled with general linear models (GLMs). The different trial phases of the object-location memory task were modeled with two regressors. One regressor was used for the retrieval phase (replacement of an object) and one for the encoding phase (following the location response, when the object was shown at

the correct location and could be collected), both of which were associated with a parametric modulator for spatial memory performance to discount large-error trials. Inter-trial-intervals (presentation of a fixation cross on a gray background) were not explicitly modeled and served as an implicit baseline. The presentation of the object cues and the feedback was modeled with two additional regressors. Furthermore, all GLMs included nuisance regressors, comprising at least 6 movement parameters, 2 regressors for signal fluctuations across white and gray matter voxels and 1 regressor to model time points with frame-wise displacements (Power et al. 2012) larger than 0.5 mm. In addition, physiological signals have been recorded for a sub-set of participants (see section below for details) which was used to correct for cardiac and respiratory artefacts by means of 14 additional regressors. The main regressors of interest modeled virtual movement periods with two associated parametric modulators (see 'Analysis of grid-cell representations' for details). Coefficients for each regressor were estimated for each participant using maximum likelihood estimates to account for serial correlations. All parametric modulators were normalized to have zero mean and thus be orthogonal to the un-modulated regressor. Prior to the second-level random effects analysis, the linear contrast images of the regression coefficients underwent nonlinear normalization to the group-specific template brain using ANTS.

Analysis of hexadirectional activity

The orientation of 6-fold rotational symmetry of entorhinal activity (referred to as 'hexadirectional activity' and consistent with grid-cell representations in humans [10]) was estimated in participant's right EC using a quadrature-filter approach on fMRI data during fast movements in all trial phases [4,5]. Participant's virtual-navigation fMRI data entered a general linear model (GLM) with two parametric modulators of a movement regressor. These modelled the sine and cosine of running direction $\theta(t)$ in periods of 60° (i.e. $\sin(6*\theta(t))$ and $\cos(6*\theta(t))$) for participant's 50% fastest movement time points, where grid-cell-like representations can be reliably detected (Doeller et al. 2010; Kunz et al. 2015). Multiplication by 6 transformed running direction into 60° periodic space to create regressors sensitive to activation showing a six-fold rotational symmetry in running direction. Activations with six evenly spaced peaks as a function of running direction will produce parameter estimates β_1 and β_2 for the two regressors with large amplitude $\mathrm{sqrt}(\beta_1^2 + \beta_2^2)$. To this end, running direction $\theta(t)$ was arbitrarily aligned to 0° of the coordinate system underlying the virtual reality engine. Participants were not aware of the environmental coordinate system. The relationship between the underlying coordinate system and the polarisation axes (defined by extra-maze cues) differed between fMRI experiment 1 and fMRI experiment 2. The orientation of the polarisation axis (i.e. 0°) had an angular offset from the underlying coordinate system of 15° in fMRI experiment 1 and 90° in fMRI experiment 2. This made it

unlikely that an anchoring of grid-cell representations to polarisation axes were due to other factors, such as viewing direction during the start of the experiment, which was -15° in fMRI experiment 1 and -90° in fMRI experiment 2, relative to the visible polarisation axes. Next, the parameter estimates of the two parametric modulators (β_1 and β_2) were extracted from the right EC ROI and used to calculate preferred orientation in 60° space (varying between 0° and 59°). A participant's mean orientation of hexadirectional activity was defined as $\varphi_{60°} = \arctan(\beta_1/\beta_2)$, where β_1 is the averaged beta value for $\sin[6*\theta(t)]$ and β_2 is the averaged beta value for $\cos[6*\theta(t)]$ across voxels of the right EC. Dividing by six transformed the mean orientation $\varphi_{60°}$ back into standard circular space of 360° for one of the three putative grid axes (the remaining two being 60° and 120° relative to the first).

Our main research question was if environmental geometry affects the orientation of putative grid-cell representations (see below for a description of the statistical test procedure). To additionally cross-validate effects of entorhinal hexadirectional activity (Doeller et al. 2010; Kunz et al. 2015; Bellmund et al. 2016), we tested the temporal stability of preferred orientations and their regional specificity in a split-half procedure (Experiment 1). This was done only for experiment 1, because data acquisition was roughly twice as long as in experiment 2, which warranted a sacrifice in sensitivity for the main research question.
The procedure involved testing activation differences in the second half of the data with six-fold rotational symmetry that was aligned with the (potentially environmentally determined) hexadirectional activity estimated from the first half of the data. More specifically, the second GLM contained regressors for both 'aligned' and 'misaligned' runs relative to the estimated hexadirectional activity (respectively, this means running directions were either less than ± 15° or more than ± 15° oriented relative to the nearest axis of hexadirectional activity). As for the estimation procedure, regressors modeling six-fold rotational symmetry captured participant's 50% fastest movement time points. Participants' contrast values (aligned > misaligned) then entered a second level random-effects analysis to test for hexadirectional activity in the entire brain volume acquired. Significant activation in the right EC would indicate temporal stability and regional specificity of putative grid orientation.
Having evaluated temporal stability and regional specificity of the quadrature-filter approach for investigation of grid-cell-like representations in fMRI experiment 1, we decided to maximise statistical power addressing the main research question of environmental effects on hexadirectional activity in fMRI experiment 2. This was deemed necessary, because fMRI experiment 2 had shorter scanning time and was conducted at lower magnetic field strength (which is associated with a smaller signal-to-noise ratio). These factors were expected to lead to a decrease in statistical power that could be alleviated by using all the data for the

estimation of putative grid orientations (using the quadrature-filter approach described above) and answering of the main research question.

Analysis of environmental anchoring of hexadirectional activity

We tested environmental anchoring of the hexadirectional activity relative to the polarisation axes by using a V test for circular homogeneity (Berens 2009). The V test for circular homogeneity is similar to the Rayleigh test for circular homogeneity and can be used if an a-priori hypothesis of a certain mean direction in a sample of angles is being tested. Due to our hypothesis of a relationship between the orientation of the grid-system and anisotropy in spatial information derived from angular changes to polarising cues, we tested participant's putative grid orientations in 0°-60° space (Figure 4B and Figure 6A) for the presence of a mean direction aligned 30° off the polarisation axis.

Author contributions:

TNS and CFD conceived the study and designed the experiments. TNS conducted and analysed the fMRI and behavioural experiments and the simulations of Euclidean triangulation. BT, NB and CB designed the biologically inspired computational models of grid cell systems for location decoding. BT conducted the simulations and analysed the results. The manuscript was written by all listed authors.

Acknowledgements

CFD and TNS's research is supported by the Netherlands Organisation for Scientific Research (NWO-Vidi 452-12-009; NWO-Gravitation 024-001-006; NWO-MaGW 406-14-114; NWO-MaGW 406-15-291), the Kavli Foundation, the Centre of Excellence scheme of the Research Council of Norway – Centre for Biology of Memory and Centre for Neural Computation, The Egil and Pauline Braathen and Fred Kavli Centre for Cortical Microcircuits, the National Infrastructure scheme of the Research Council of Norway – NORBRAIN, and the European Research Council (ERC-StG RECONTEXT 261177; ERC-CoG GEOCOG 724836).

CB, NB and BWT's research is supported by the Wellcome Trust. CB's research is also supported by the Royal Society. The authors would like to thank A Backus, J Bellmund, P Medendorp and B Milivojevic for useful discussions, A. Vicente-Grabovetsky for help with data analyses, B Somai for help with optimising the behavioural paradigm and C Hutton for support with the physiological noise correction.

Figures:

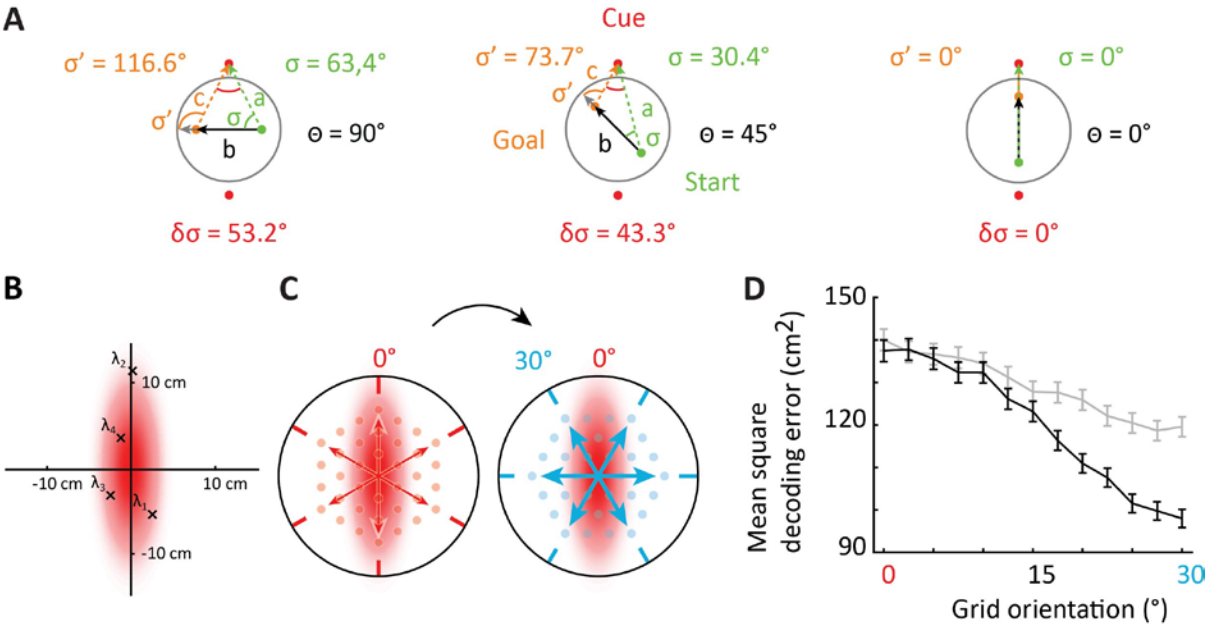

Figure 1. Spatial information is anisotropic and affects optimal self-localisation using grid cells. A Spatial information during movement in polarised environments is anisotropic. Three example paths in different directions and through the center are shown (black arrows at angle θ; Path lengths are equal to distance of the cue to the center). The change in cue direction from the observer's heading (δσ) is maximal on paths perpendicular to the polarisation axis. **B-D** We simulated decoding of position estimates from the activity of grid cell ensembles with patterns oriented at different angles relative to the axis of lowest spatial certainty. Uncertainty in spatial information was introduced by adding Gaussian errors to the position information input to the grid cells. These errors were generated independently for each module of grid cells. Anisotropy was created by separately varying the standard deviations of the error in two orthogonal axes. **B** illustrates an example: the subject's actual location is at the origin; red shading indicates a two-dimensional probability density distribution for error generation, with different standard deviations in each axis; and crosses indicate four independently generated noisy position estimates, drawn from this distribution and be input to each of the grid cell system's four modules. **C** Schematic illustration of two grid orientations either aligned with the uncertainty axis (left panel, arrows indicate hexadirectional orientations associated with a grid), or rotated 30° (right panel). The number of depicted grid fields differ only for illustration purpose. **D** Position decoding error, defined as the mean maximum-likelihood estimate square error (MMLE; cm^2), was largest when one grid axis was aligned at 0° (as shown in panel B, left side). Solid black: errors with s.d. 5cm and 0cm; dashed grey line: 5cm and 1.67cm. Grid orientation is defined as the minimal angular offset of a grid axis from the axis of greater uncertainty (this is analogous to hexadirectional offset of entorhinal fMRI activity described below). Error bars indicate 95%

confidence interval (n=150,000).

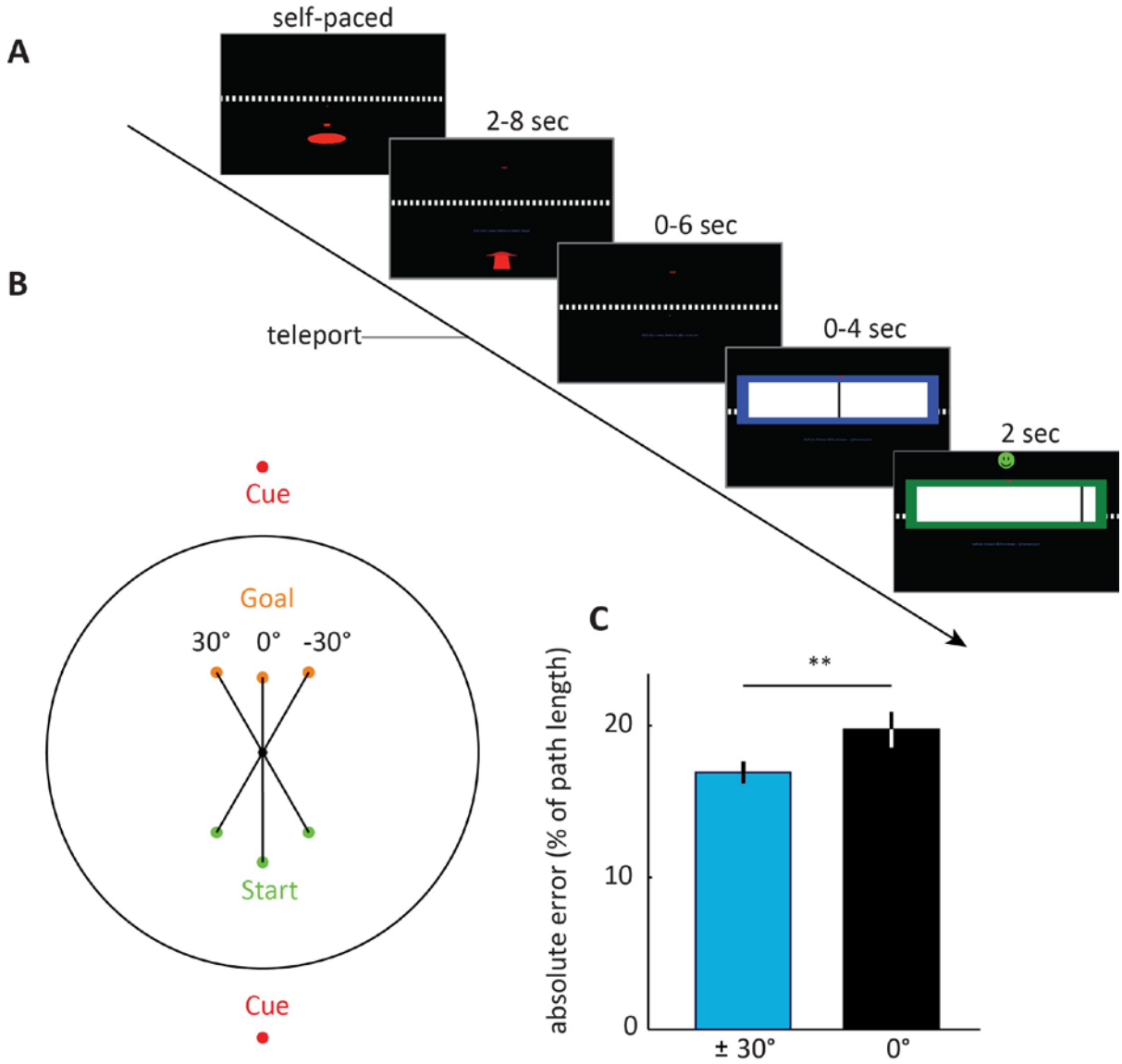

Figure 2. Distance estimation is most accurate on oblique paths. A Trial event sequence. Following a familiarisation phase, participants navigated to a start location and initiated teleportation in a given direction, either along a polarisation axis or at ±30° offset, see B and Figure S4. Teleportation distance was experimentally manipulated and participants gave a distance estimate at the goal location by sliding a response bar (black slider in blue box). The cue was visible both at the start and the goal location. Subsequently, participants received feedback. **B** Schematic of the three possible path angles shown at the same distance. Path distance varied from trial to trial (see Experimental Procedures). Note that no boundary was present. The black circle only illustrates an analogy to the arena environments used in the fMRI experiments. Start and goal positions are illustrated by green

and orange dots, respectively. **C** Distance estimation was most accurate on oblique paths, consistent with anisotropy of spatial information.

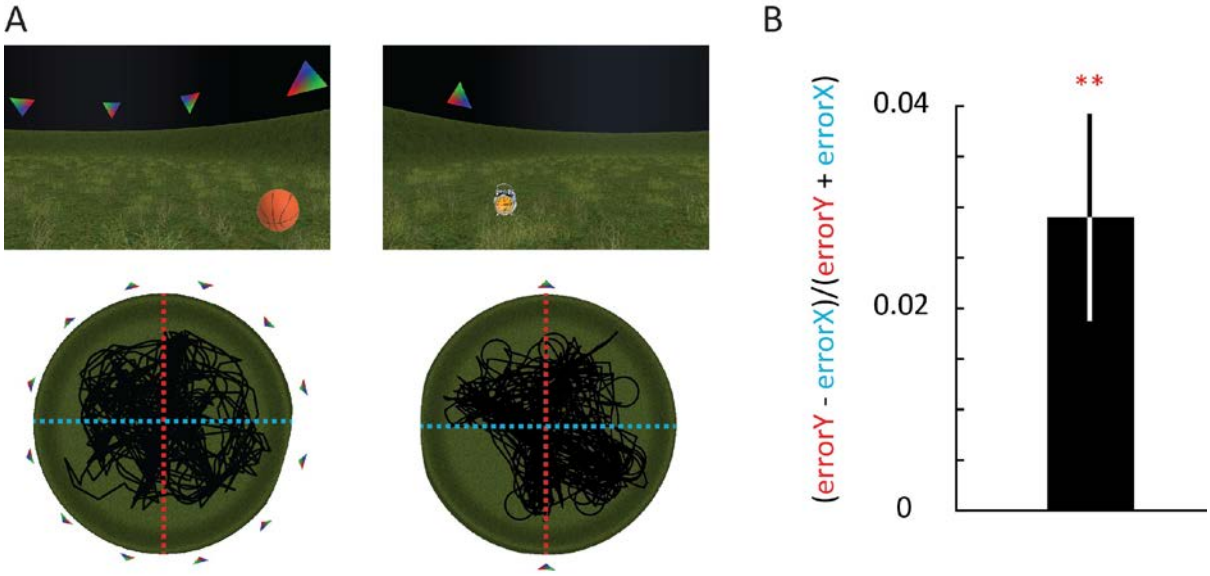

Figure 3. Spatial memory performance is anisotropic. A Virtual environments used in the fMRI studies. First person (top) and aerial (bottom) view of the virtual environments used in experiment 1 (left) and experiment 2 (right). Human participants performed a free-navigation, object-location memory task (one example object shown on grassy plane, see Experimental Procedures). In experiment 1, an implicit polarisation axis was defined through the configuration of cues, i.e. the switch between upright and downward triangles. In experiment 2, an explicit polarisation axis was defined with two triangular cues alone. Black lines in aerial view show the paths of two exemplary participants. Red dashed line indicates the polarisation axis (Y dimension), whereas the cyan dashed line indicates the orthogonal X dimension. **B** Mean spatial memory error in virtual units (vu) was larger along the Y dimension (i.e. the polarisation axis) than along the X dimension. The anisotropy was quantified as (Y-X)/(Y+X). This measure yields positive values if the error on the Y dimension are larger than on the X dimension. This anisotropy in spatial memory performance corroborates the theoretical predictions of an anisotropy in spatial information (Equation 1, Figure 1 and Figure S1).

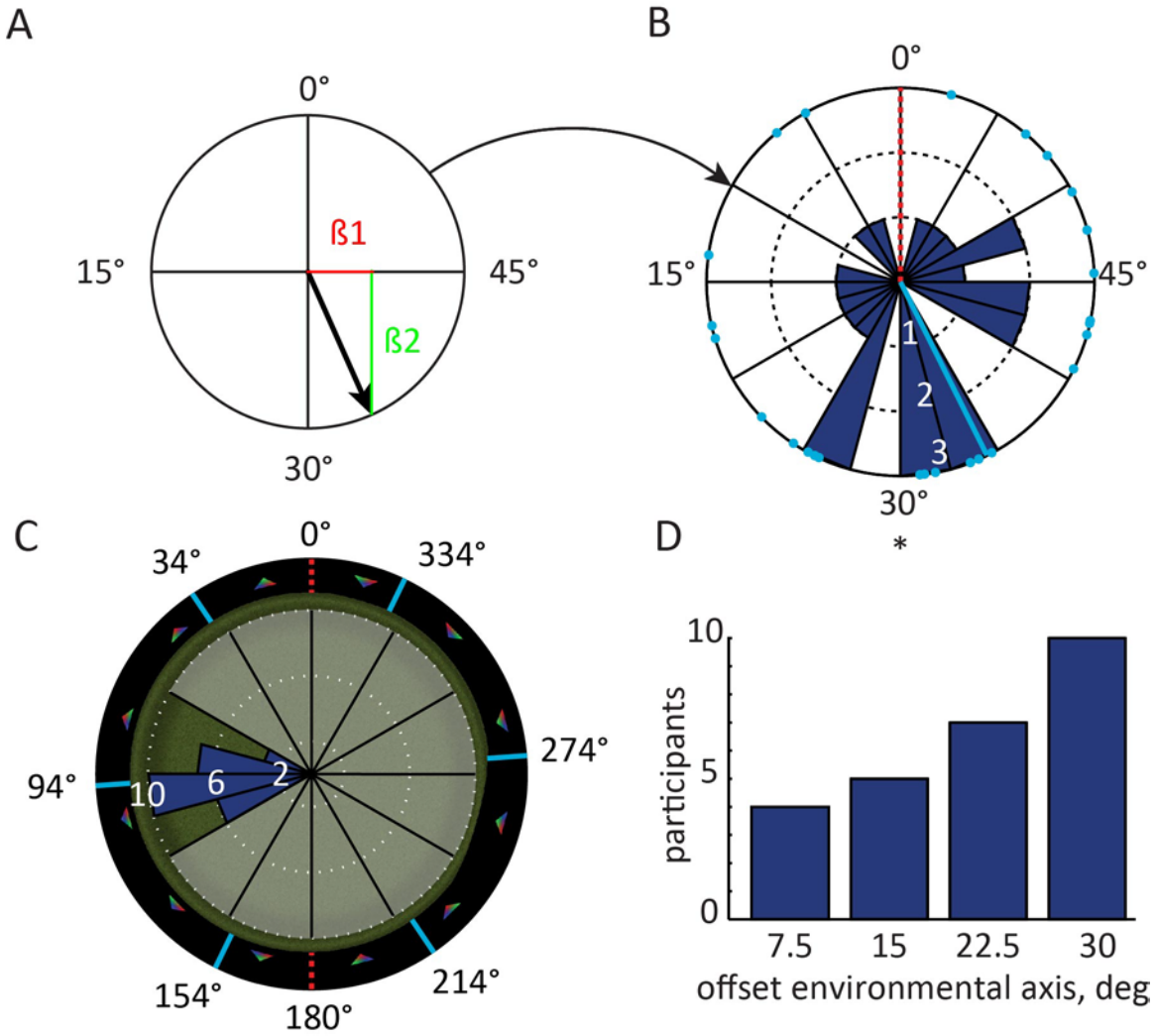

Figure 4. Hexadirectional activity in entorhinal cortex aligns perpendicular to the polarisation axis. A Analysis procedure: the preferred orientation of hexadirectional fMRI activity in the entorhinal cortex was estimated by first fitting a general linear model (GLM) to the data with 60°-periodic sine and cosine regressors. This yields the associated parameter estimates ß1 and ß2, respectively. The preferred orientation in 60°-space (black arrow) can be derived from ß1 and ß2 (see Experimental Procedures). The corresponding preferred orientation of hexadirectional activity in 360°-space can then be deduced. Here, this corresponds to multiples of 60° centered on 34° (light blue lines in C) relative to the polarisation axis (red dashed line) at 0°. **B** Individual, preferred orientations in 60°-space (light blue dots) in right entorhinal cortex clustered at roughly 30° offset relative to the polarisation axis; mean orientation = 34° (light blue line). **C** Histogram of preferred hexadirectional activity plotted in full circular space (360°). Note that one of the hexadirectional axes is roughly orthogonal to the polarisation axis, in line with optimal angles for self-localisation (Figure 1D) **D** Absolute angle between nearest axis of hexadirectional activity shown in B and the polarisation axis illustrate a tendency towards maximal

misalignment. Note that the maximum offset is 30° due to the 60° periodicity of hexadirectional activity.

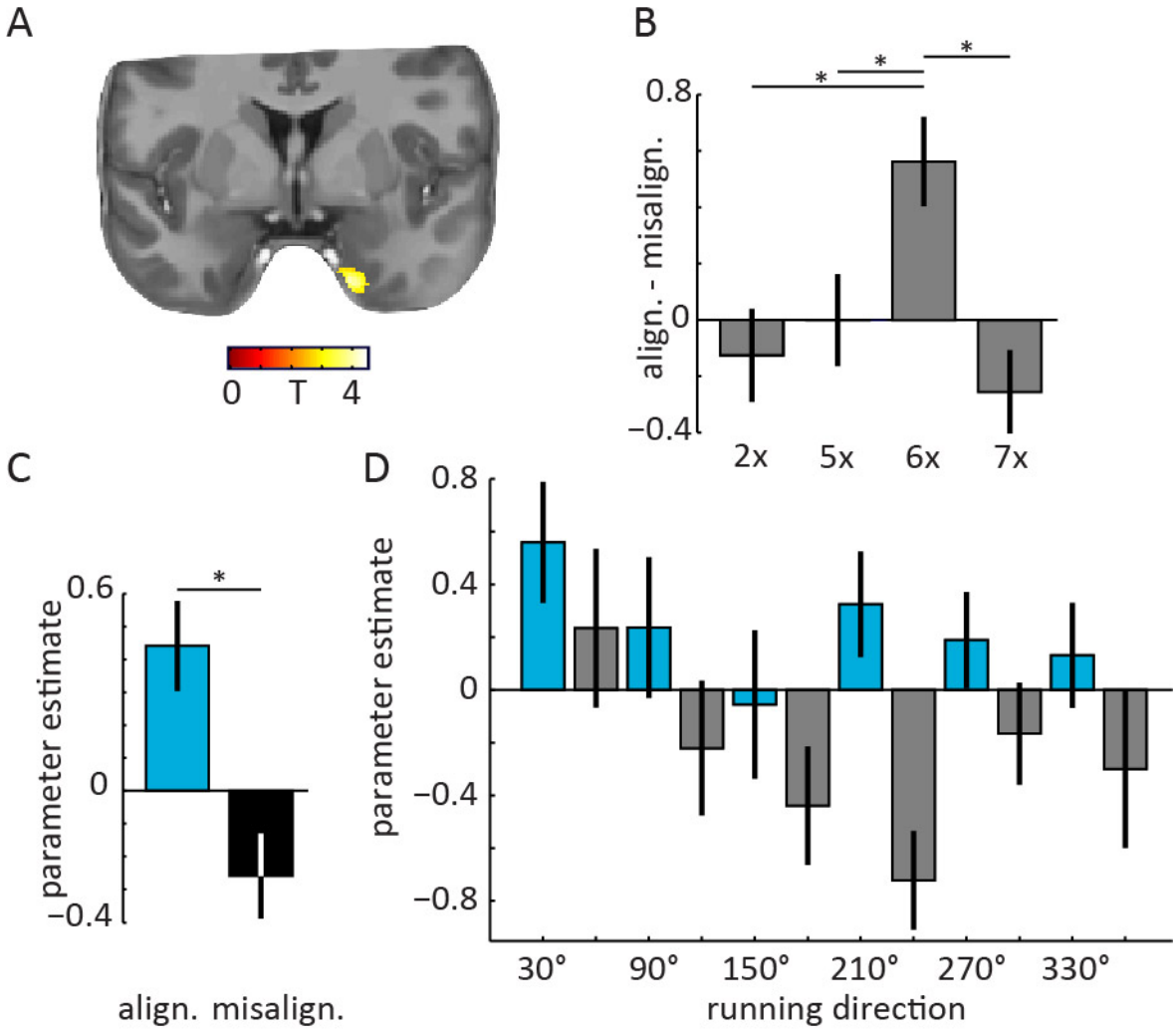

Figure 5. Cross-validation of hexadirectional activity in entorhinal cortex and control models. A A whole-brain cross-validation confirmed that entorhinal activity was increased on runs aligned with the predicted grid (i.e. runs in 30°-wide bins centered on 30°, 90°, 150° etc. indicated by light blue arrows in C and D; see Experimental Procedures for details). Image is thresholded at p<0.001 uncorrected for display purpose. Effects are significant at T(25) = 4.44, small-volume FWE-corrected p=0.034. The T statistic (colour bar) is overlaid on the structural template. Across the cerebrum no other peaks were observed at p<0.001, uncorrected. **B** In agreement with grid-cell-like representations, runs aligned versus misaligned show largest activity increase for 6-fold (6x) rotational symmetry but not for biologically implausible control models. Next to 5- and 7-fold rotational symmetry, 2-fold symmetry was tested to rule out a direct effect of running parallel to the polarisation axis or not. For all analyses the aligned condition was centered at an angle equivalent to 90° from the polarisation axis (e.g. 30° for 6-fold symmetry). **C** Parameter estimates of runs aligned (light blue, see schematic grid in Figure 1C right panel) and misaligned (black) with the

predicted hexadirectional orientation extracted from the peak voxel in A. **D** To examine the influence of different running directions, we plotted the parameter estimates for separate regressors of 12 directional across the entire time-series of fMRI data from the peak-voxel in A. Note the alternating pattern of activity aligned and misaligned. Bars show means and SEM across participants.

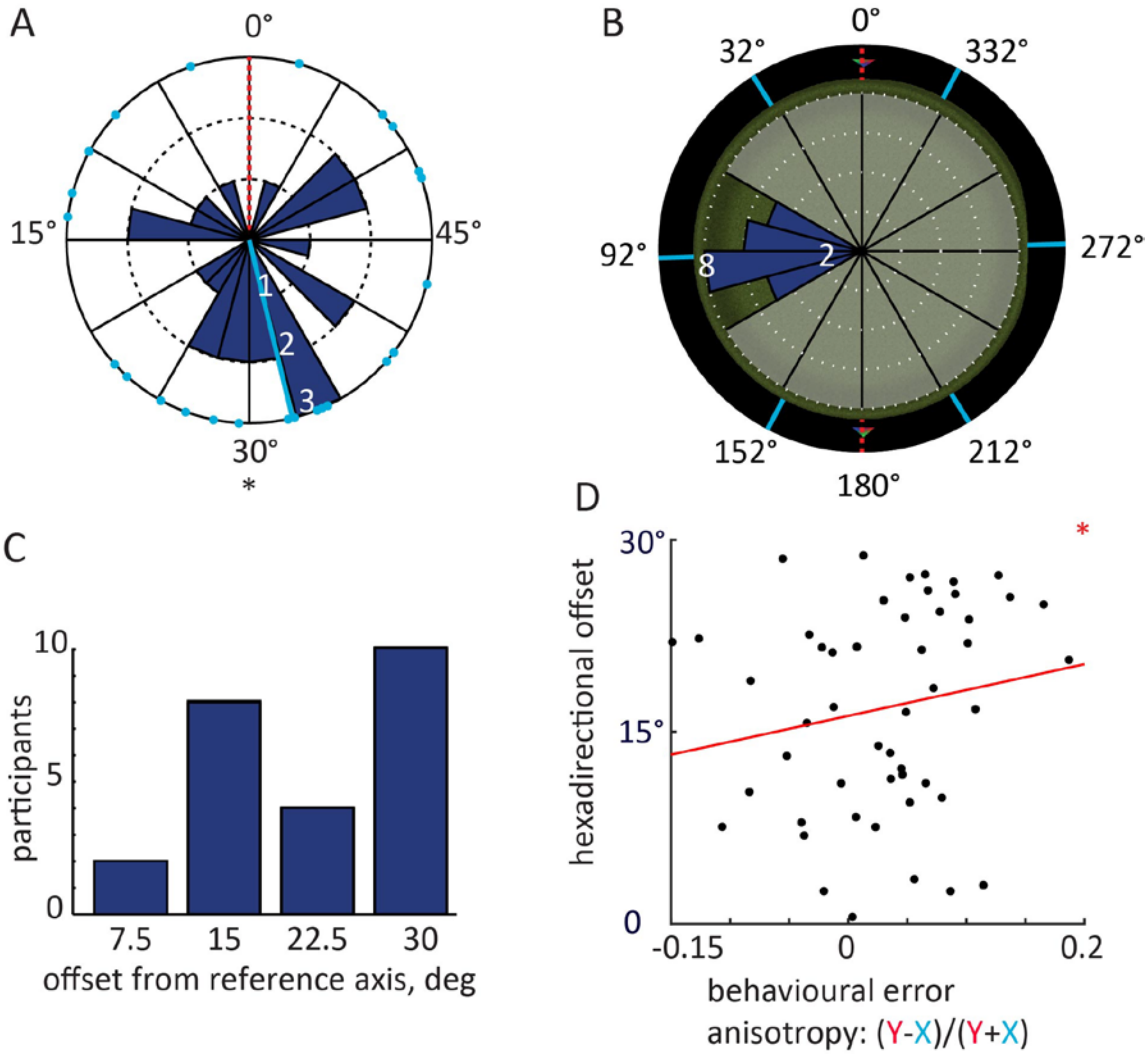

Figure 6. Environmental effects on hexadirectional activity in experiment 2 and correlation with behaviour. A Preferred hexadirectional activity in 60°-space (light blue dots) in right entorhinal cortex clustered at roughly 30° offset relative to the polarisation axis(light blue line), in line with optimal angles for self-localisation (Figure 1D) **B** Histogram of preferred hexadirectional orientations plotted in full circular space (360°) onto a top-down view of the arena. Note that one of the putative grid axes is roughly orthogonal to the polarisation axis. **C** Absolute angle between nearest axis of hexadirectional activity shown in B and the polarisation axis. Note that the maximum offset is 30° due to the 60° periodicity of hexadirectional activity. **D** Hexadirectional offset correlates with anisotropy in spatial memory

performance across participants. The positive relationship indicates that participants with a more orthogonal orientation of hexadirectional activity were relatively more precise in placing objects on the X dimension than the Y dimension.

SUPPLEMENTAL INFORMATION

Supplemental Figures:

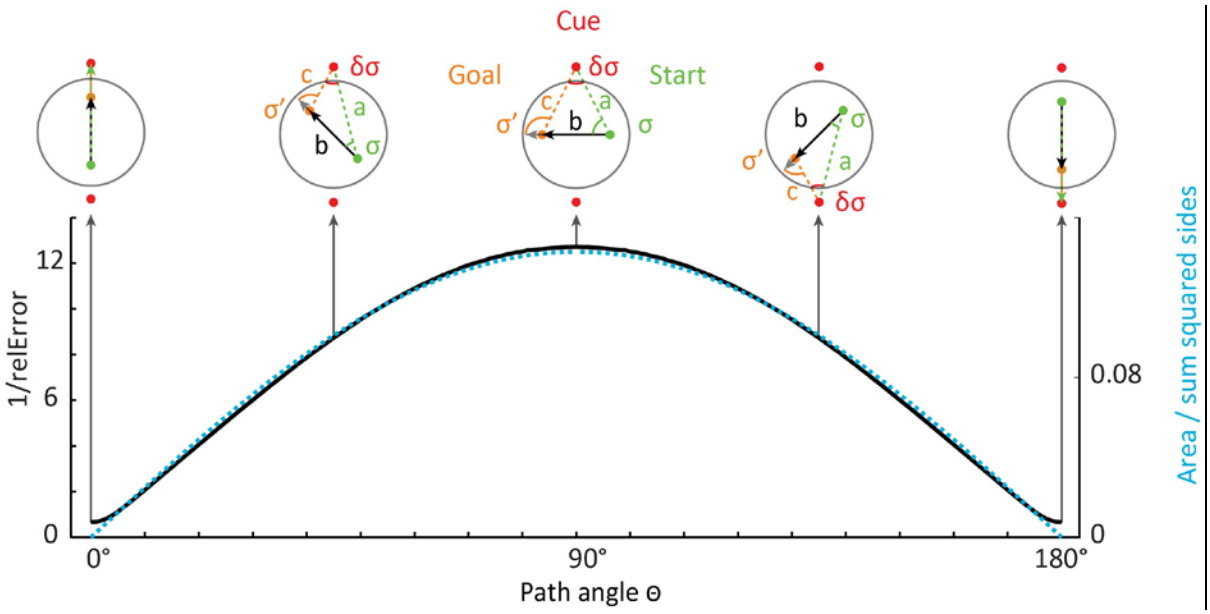

Figure S1. Triangulation under noise in circular and square environments. To test the impact of anisotropic optic flow information on spatial computations, we performed a biologically inspired simulation of Euclidean triangulation. For example, an estimate of the distance between start and end points was computed from noisy estimates of the angles and distance to one of the cues using equation 2. All sides (a-c) of a triangle served as both inputs and distance to be estimated, before the results were averaged on one iteration. The median noise resilience (1/relative error [relError]) across iterations is plotted in black. On a given iteration, relErr is determined as the absolute distance error / side length, averaged across the three sides of each triangle. Black arrows indicate example paths between two observer positions (start in green and goal in orange, always crossing the center; see Experimental Procedures for details). Red dots show polarising cues. Most precise triangulation was achieved on paths orthogonal to the polarisation axis ($10*10^3$ repetitions for each triangle, 90° ±15° versus 0° ±15°, two-sided Wilcoxon signed-rank test: $Z=1026.42$, $p<0.001$). Optimal path angle was well predicted by a quality measure for triangulation (triangle area / sum of squares of the side lengths; $R=0.99$, $p<0.001$). This measure increases for more equilateral triangles.

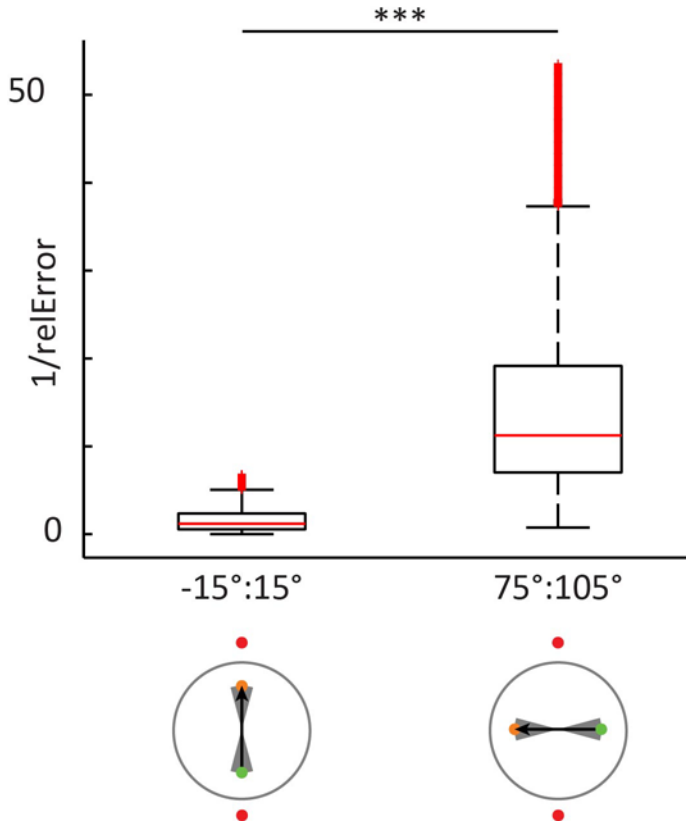

Figure S2. Magnitude of noise resilience of directional bin of paths centered on peaks and troughs of Figure S1. The most accurate triangulation was achieved on paths orthogonal to the polarisation axis. $10*10^3$ repetitions for each triangle, 90° ±15° versus 0° ± 15°, two-sided Wilcoxon signed-rank test: Z=1026.42, p<0.001. The gray shaded area in the bottom panels indicate the range of paths that were tested. The box edges denote the 25th and 75th percentiles and central red mark the median. The whiskers extend maximally to $q_3 + 1.5 * (q_3 - q_1)$ and minimally to $q_1 - 1.5 * (q_3 - q_1)$, where q_1 and q_3 are the 25th and 75th percentiles, respectively. A red + denotes points outside this range, with the exception of the upper 10% of values that were omitted for display purposes. Statistical testing included all data.

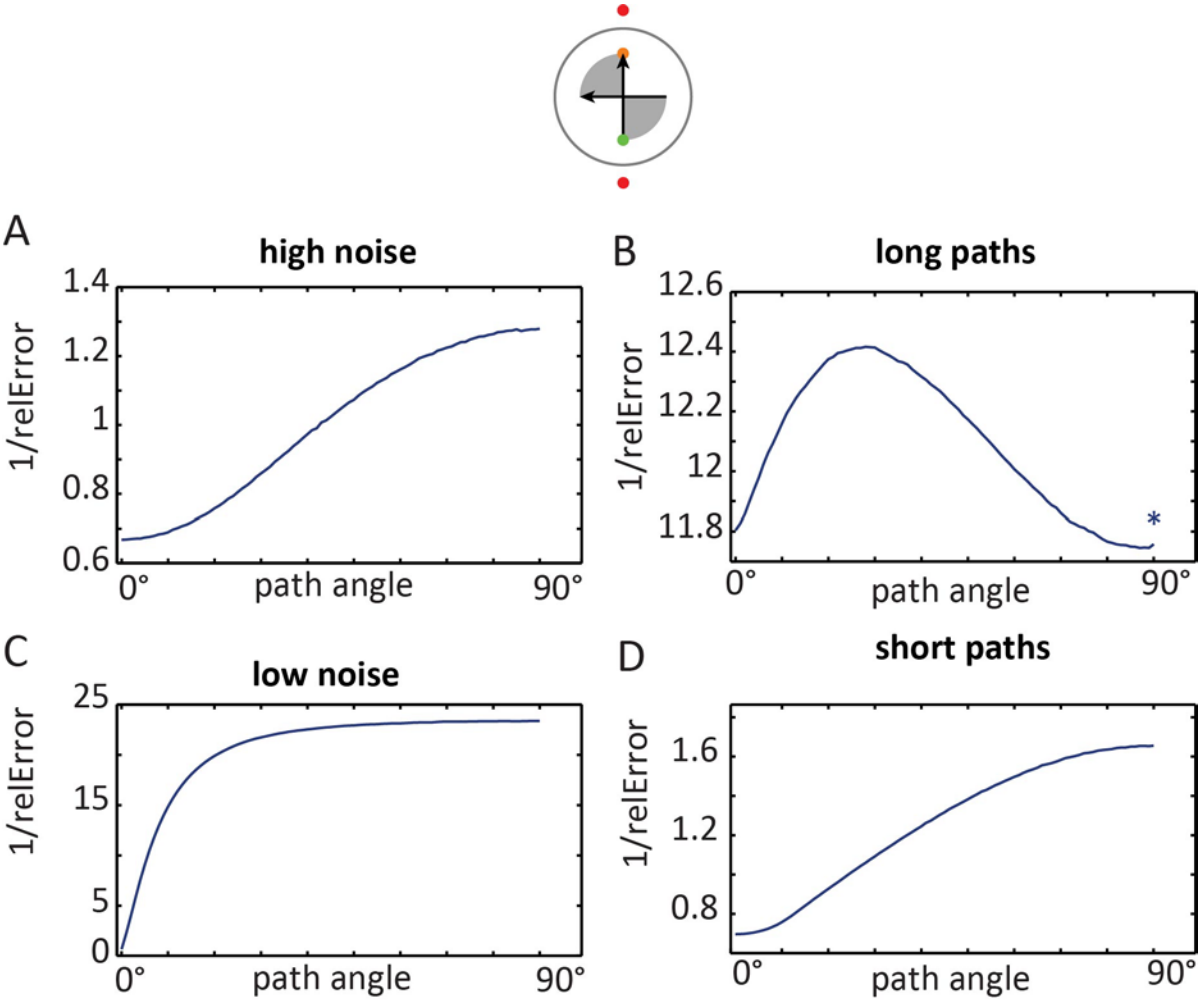

Figure S3. Effects of noise levels and path length on optimal triangulation paths Environment with a single axis are defined by two cues (analogous to the two fMRI experiments and the behavioural experiment). All (A, C, D) except the long path condition (B) yielded an optimum at 90°. However, this extreme case never occurred for participant's paths in the fMRI experiments due to the limitations of the circular boundary. The average length of straight (+-45°) paths was 11% of the polarisation axis' length in fMRI experiment 1 (12% in fMRI experiment 2) – See Figure S6E-F. High noise = randomly sampled from a distribution with a 10 times larger sigma (62.6, instead of 6.26, see Experimental Procedures). Low noise = randomly sampled from a distribution with a 10 times smaller sigma (0.626, instead of 6.26). Long paths = simulated path length was equal to the length of the polarisation axis (instead of 50%, see Experimental Procedures). Short paths = simulated path length was 5% of the length of the polarisation axis (instead of 50%, see Experimental Procedures). Asterix = plots have been smoothed with a 5°-wide kernel for display purposes. The gray shaded area in the top panels indicates the range of paths that were used.

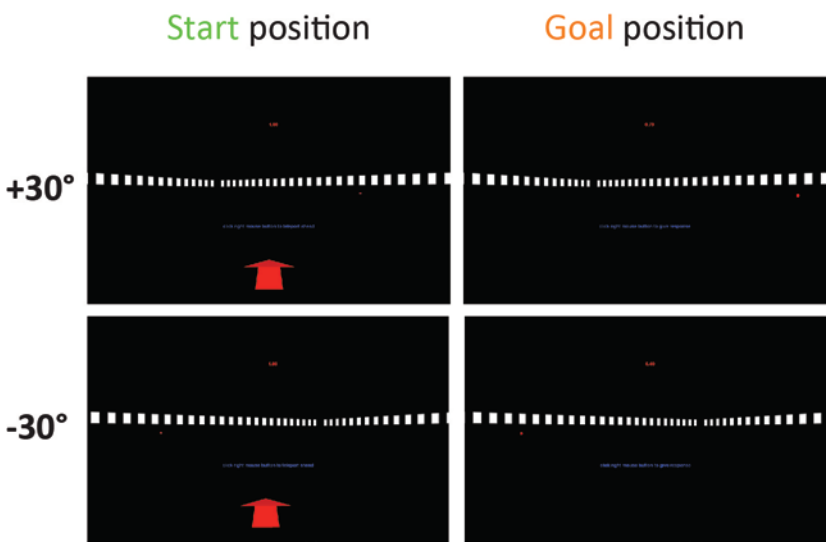

Figure S4. Additional views of the behavioural experiment at the beginning (Start) and end (Goal) of a path. Note that the background was rendered at infinity (see Experimental Procedures), such that it did not change during translations in the ±30° or the 0° condition (Figure 2BC).

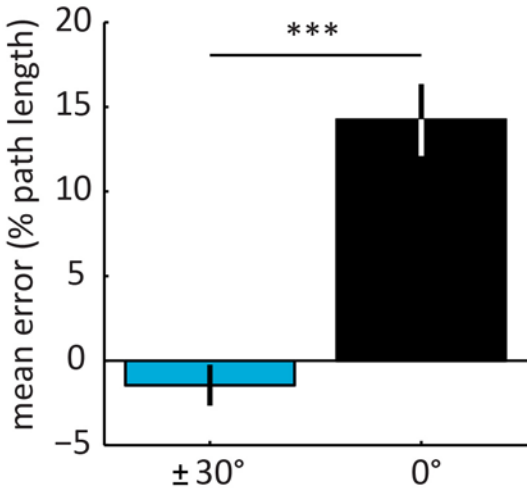

Figure S5. Accuracy (mean estimation error in percent of correct path length) in the behavioural experiment (Figure 2)**.** Paths along the polarisation axis (0°) yielded less accurate distance estimation than oblique paths (±30°). Paired, two-sided t-test N=20; T(19) = 5.47, p<0.001. See Figure 2C for an effect in the same direction for precision (absolute error). Bars show errors in percent of correct path length averaged across participants +-SEM; Mean 0° condition = 11.8 %; Mean ±30° condition= -0.8 %.

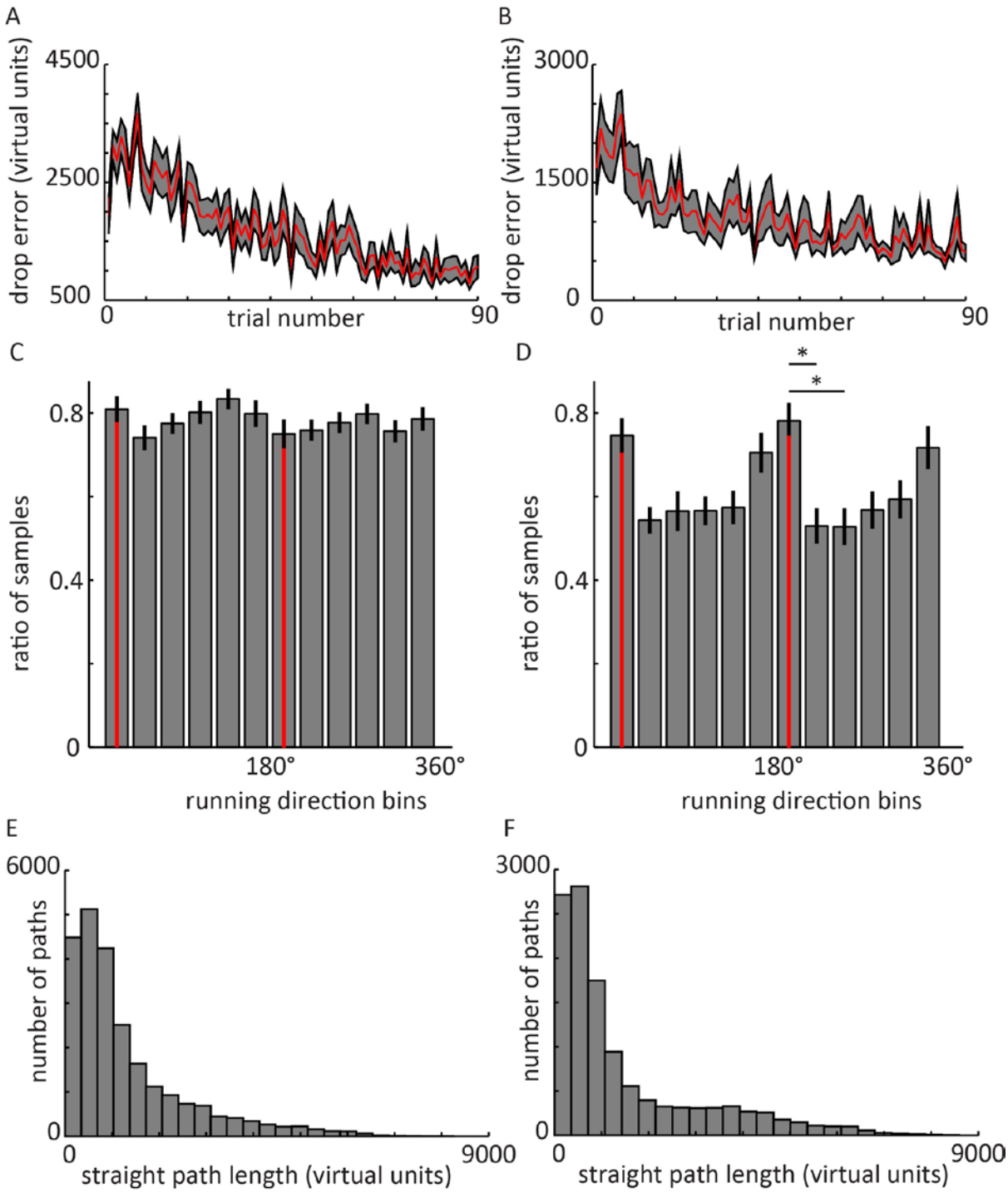

Figure S6. Behavioural analyses of fMRI experiment 1 (A, C, E) and fMRI Experiment 2 (B, D, F). Spatial memory performance: the decreases in drop error indicate that participants in both experiments were able to successfully navigate and remember locations in the sparse virtual environments. Participants learned the locations of 6 objects in fMRI experiment 1 (A) and 4 objects in fMRI experiment 2 (B; See Experimental Procedures). Red line denotes mean drop error (i.e. Euclidean distance in virtual units between participants'

response location and the correct location of a given object on a given trial) across participants. Gray outline denotes standard error of the mean. For display purposes, results are shown up to trial number 90 for consistency. Variations in the number of trials across participants were due to differences in self-paced completion of trials. **C-D** Sampling of running directions. The number of samples of movements in 30° bins of running direction was normalised within participants for comparability across participants by dividing it by the maximum number of samples in any of the 12 bins, thereby yielding a maximum value of 1 for a bin. **C** FMRI experiment 1 (polarisation axis defined by configural cues), N = 26: A non-parametric Friedman test of median differences among repeated measures of directional sampling was conducted and resulted in a Chi-square value of 9.5, which was not significant ($p=0.57$). **D** FMRI experiment 2 (polarisation axis defined by non-configural cues), N = 24: A non-parametric Friedman test of median differences among repeated measures was conducted and resulted in a Chi-square value of 36.7, which was significant ($p<0.001$). Post-Hoc tests with Tukey-Kramer correction for multiple comparisons revealed that particularly runs along the environmental axis at 165° (+-15°) occurred more often than runs oblique at 195° (+-15°) and 125° (+-15°). Asterix: $p<0.05$ Note that both the absence of a difference in fMRI experiment 1, as well as more frequent runs along the polarisation axis in fMRI experiment 2 speak against the possibility that the environmental effects on hexadirectional activity reported above would be due to biases in navigation behaviour. **E-F** Distances of running paths. Histograms show the number of straight paths for different distances. Path length was determined as the Euclidean distance between start and end point of a path with continuous movement and rotations of less than +- 45° (i.e. a 90°-wide bin). FMRI experiment 1 (E): mean = 1316.2 vu. FMRI experiment 2 (F): mean = 1493.5 vu.

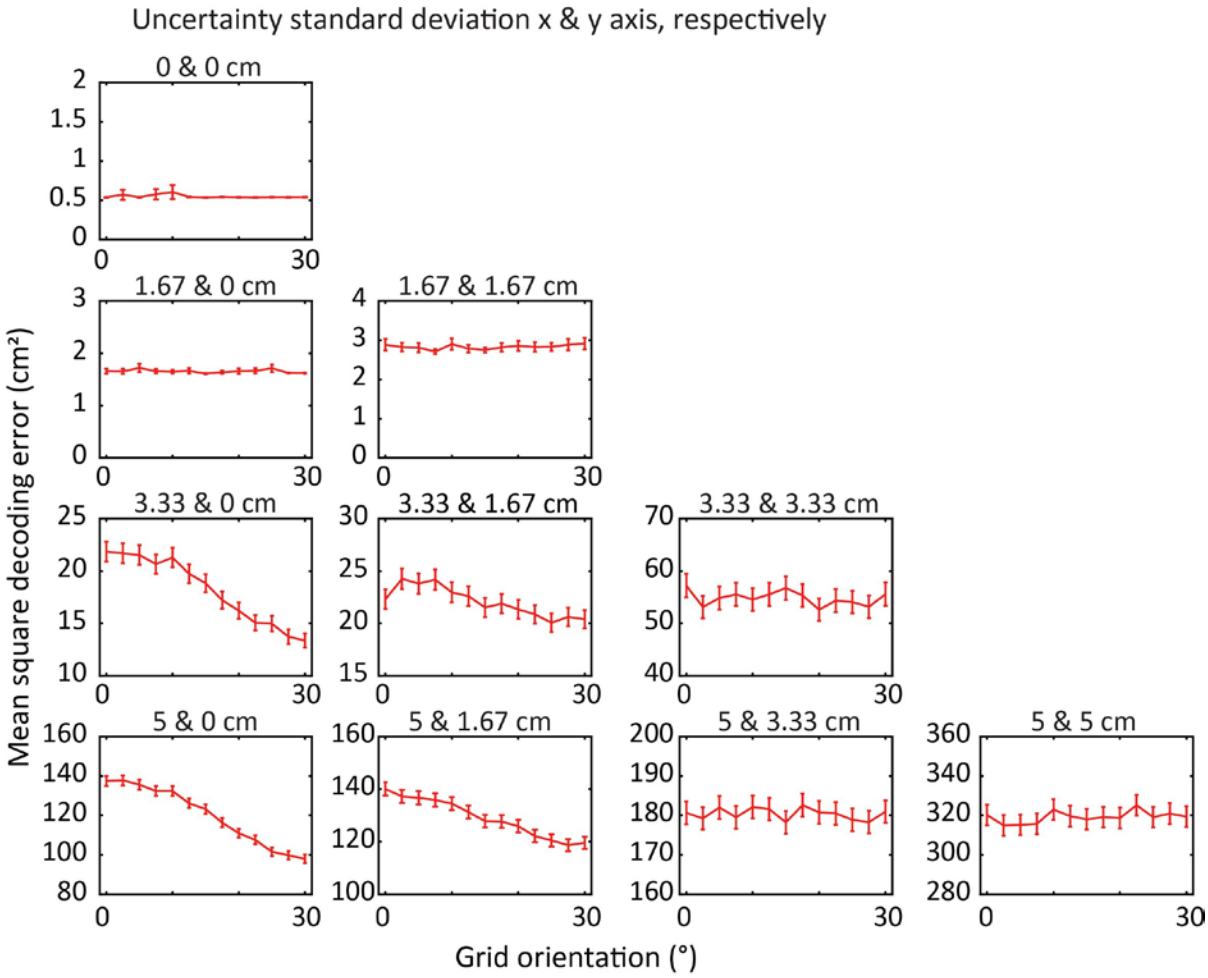

Figure S7. More extreme anisotropy in spatial uncertainty results in a more pronounced dependency of self-localisation accuracy on grid orientation. The performance of grid cell systems was assessed while independently varying the degrees of spatial uncertainty in two orthogonal axes. When uncertainty is equal in both axes performance does not depend on the orientation of the grid pattern. As uncertainty becomes more anisotropic, self-localisation is more accurate in grid cell systems in which the grid pattern axes are aligned away from the axis of greatest spatial uncertainty.

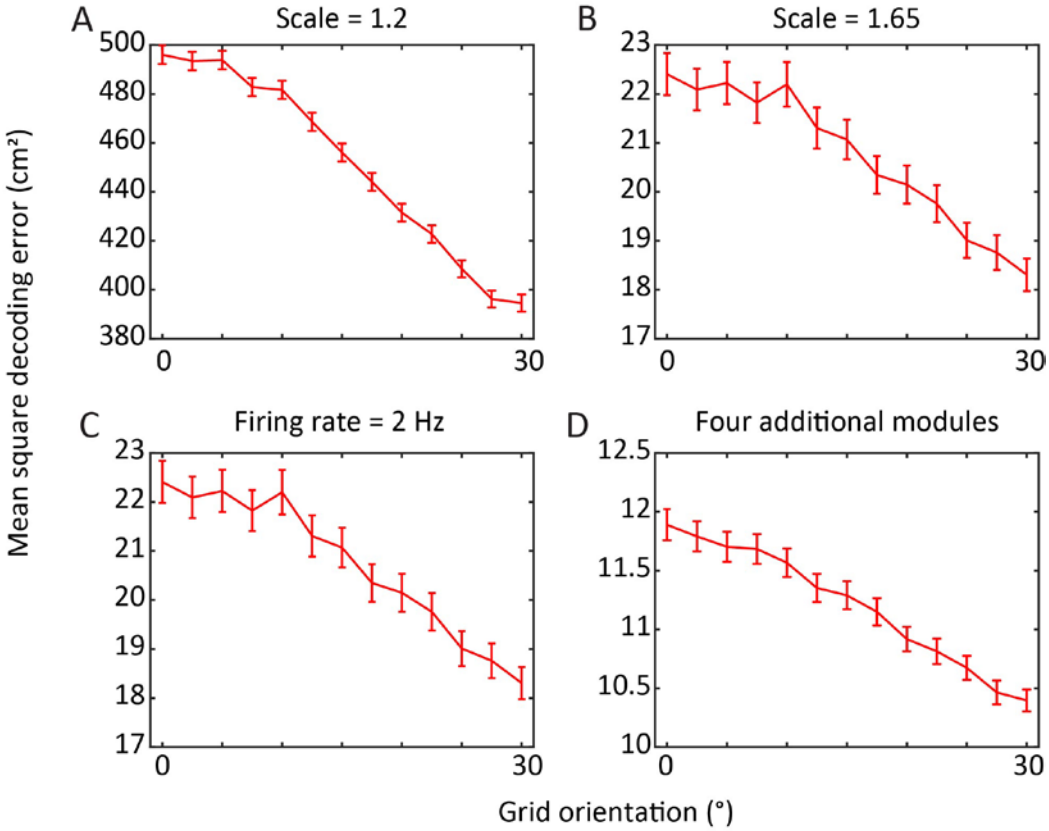

Figure S8. The dependency of self-localisation accuracy on grid orientation is stable within reasonable sets of grid cell system parameters. Performance is consistently best when the grid axes are aligned away from the axis of least spatial uncertainty, across variations in the parameters of the grid cell system. Error bars indicate 95% confidence interval, n = 150,000 unless otherwise specified. **A** Grid period scaling factor reduced to 1.2. **B** Grid period scaling factor increased to 1.65**. C** Grid cell maximum firing rate reduced to 2Hz. (In order to compensate for increased effects of noise in this system, the number of cells per module was quadrupled. Due to the high computational intensity of this simulation n = 75,000.) **D** Four further grid cell modules added, with scales continuing to increase geometrically.

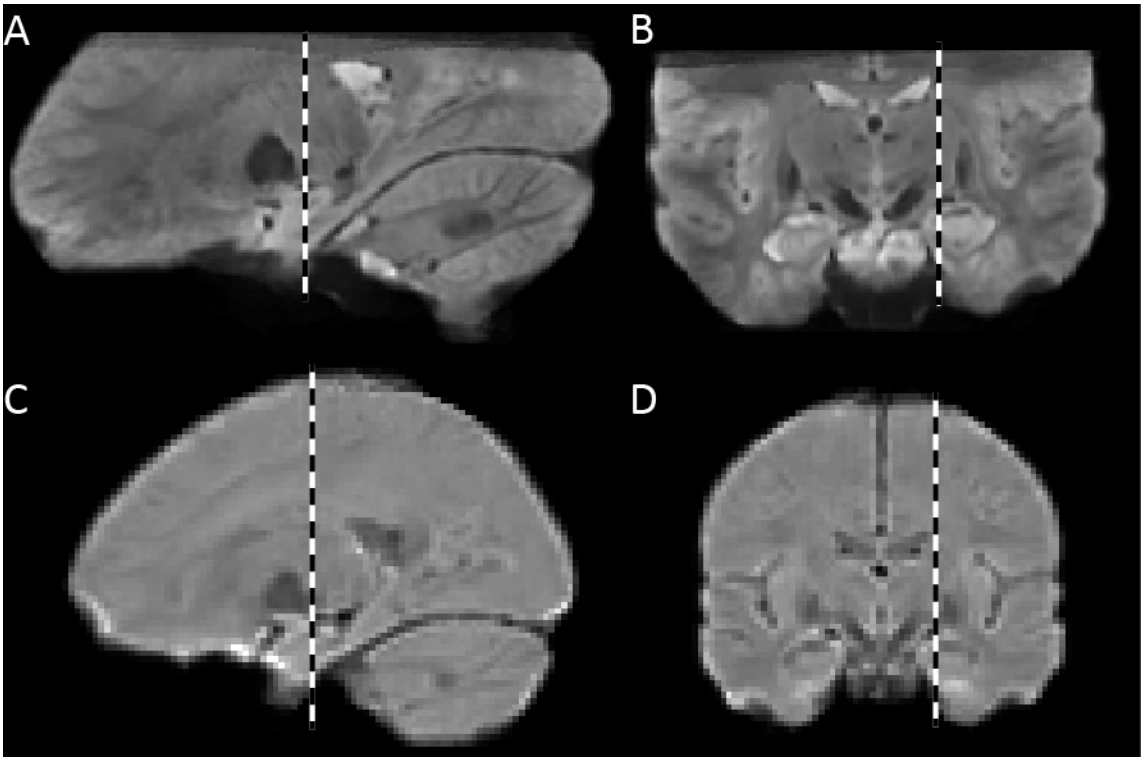

Figure S9. Mean functional images across participants used as template brains. A-B Template for fMRI experiment 1 (7T scanner). **C-D** Template for fMRI experiment 2 (3T scanner). Dashed lines indicate the location of the slice in the corresponding orientation in the panel above or below. Template images were created with Advanced Neuroimaging Toolbox (ANTS; http://www.picsl.upenn.edu/ANTS/) based on individual, mean 3D echo-planar images. Note the relatively high contrast for functional images in the 7T data, with clear grey and white matter intensity differences even in the medial temporal lobes.

References

Amunts, K. et al., 2000. Brodmann's areas 17 and 18 brought into stereotaxic space-where and how variable? *NeuroImage*, 11(1), pp.66–84.

Amunts, K. et al., 2005. Cytoarchitectonic mapping of the human amygdala, hippocampal region and entorhinal cortex: intersubject variability and probability maps. *Anatomy and embryology*, 210(5–6), pp.343–52.

Bach, D.R. & Dolan, R.J., 2012. Knowing how much you don't know: a neural organization of uncertainty estimates. *Nature Reviews Neuroscience*, 13, pp.572–586.

Bank, R.E. & Smith, R.K., 1997. Mesh Smoothing Using A Posteriori Error Estimates. *SIAM Journal on Numerical Analysis*, 34, pp.979–997.

Barry, C. et al., 2007. Experience-dependent rescaling of entorhinal grids. *Nature Neuroscience*, 10(6), pp.682–684.

Barry, C., Ginzberg, L.L., et al., 2012. Grid cell firing patterns signal environmental novelty by expansion. *Proceedings of the National Academy of Sciences*.

Barry, C., Heys, J.G. & Hasselmo, M.E., 2012. Possible role of acetylcholine in regulating spatial novelty effects on theta rhythm and grid cells. *Frontiers in Neural Circuits*, 6, pp.1–13.

Bellmund, J.L.S. et al., 2016. Grid-cell representations in mental simulation. *eLife*, pp.1–21.

Berens, P., 2009. CircStat: A MATLAB toolbox for circular statistics. *Journal of Statistical Software*, 31(10), pp.1–21.

van Bergen, R.S. et al., 2015. Sensory uncertainty decoded from visual cortex predicts behavior. *Nature Neuroscience*, 18(12), pp.1728–1730.

Burak, Y. & Fiete, I.R., 2009. Accurate Path Integration in Continuous Attractor Network Models of Grid Cells O. Sporns, ed. *PLoS Computational Biology*, 5(2), p.e1000291.

Bürgel, U. et al., 2006. White matter fiber tracts of the human brain: Three-dimensional mapping at microscopic resolution, topography and intersubject variability. *NeuroImage*, 29(4), pp.1092–1105.

Burgess, C.P. & Burgess, N., 2014. Controlling Phase Noise in Oscillatory Interference Models of Grid Cell Firing. *Journal of Neuroscience*, 34(18), pp.6224–6232.

Burgess, N., 2006. Spatial memory: how egocentric and allocentric combine. *Trends in Cognitive Sciences*, 10(12), pp.551–557.

Burgess, N., Barry, C. & O'Keefe, J., 2007. An oscillatory interference model of grid cell firing. *Hippocampus*, 17(9), pp.801–812.

Bush, D. et al., 2015. Using Grid Cells for Navigation. *Neuron*, 87(3), pp.507–520.

Bush, D., Barry, C. & Burgess, N., 2014. What do grid cells contribute to place cell firing ?

Trends in Neurosciences, pp.1–10.
Carpenter, F. et al., 2015. Grid Cells Form a Global Representation of Connected Environments. *Current Biology*, 25(9), pp.1176–1182.
Carpenter, F. & Barry, C., 2016. Distorted Grids as a Spatial Label and Metric. *Trends in Cognitive Sciences*, pp.2–5.
Chen, G. et al., 2016. Absence of Visual Input Results in the Disruption of Grid Cell Firing in the Mouse. *Current biology : CB*, pp.1–8.
Crone, G.R., 1953. *Maps and their makers: an introduction to the history of cartography*, Hutchinson's University Library, London, New York.
Daw, N.D. & Dayan, P., 2014. The algorithmic anatomy of model-based evaluation. *Philosophical transactions of the Royal Society of London. Series B, Biological sciences*, 369(1655), p.20130478-.
Derdikman, D. et al., 2009. Fragmentation of grid cell maps in a multicompartment environment. *Nature neuroscience*, 12(10), pp.1325–32.
Doeller, C.F., Barry, C. & Burgess, N., 2010. Evidence for grid cells in a human memory network. *Nature*, 463(7281), pp.657–61.
Elliott, D., 1987. The influence of walking speed and prior practice on locomotor distance estimation. *Journal of motor behavior*, 19(4), pp.476–485.
Epstein, R.A., 2008. Parahippocampal and retrosplenial contributions to human spatial navigation. *Trends in cognitive sciences*, 12(10), pp.388–96.
Erdem, U.M. & Hasselmo, M.E., 2013. A Biologically Inspired Hierarchical Goal Directed Navigation Model. *Journal of physiology, Paris*.
Gibson, J.J., 1958. Visually controlled locomotion and visual orientation in animals. *British journal of psychology (London, England : 1953)*, 49(3), pp.182–194.
Giocomo, L.M. & Hasselmo, M.E., 2008. Computation by oscillations: implications of experimental data for theoretical models of grid cells. *Hippocampus*, 18(12), pp.1186–99.
Hafting, T. et al., 2005. Microstructure of a spatial map in the entorhinal cortex. *Nature*, 436(7052), pp.801–6.
Hardcastle, K., Ganguli, S. & Giocomo, L.M., 2015. Environmental Boundaries as an Error Correction Mechanism for Grid Cells. *Neuron*, pp.1–13.
Horner, A.J. et al., 2016. Grid-like Processing of Imagined Navigation. *Current Biology*, pp.1–6.
Howard, L.R. et al., 2014. The Hippocampus and Entorhinal Cortex Encode the Path and Euclidean Distances to Goals during Navigation. *Current Biology*, pp.1–10.
Hutton, C. et al., 2011. The impact of physiological noise correction on fMRI at 7T. *NeuroImage*, 57(1), pp.101–112.

Kiani, R. & Shadlen, M.N., 2009. Representation of confidence associated with a decision by neurons in the parietal cortex. *Science (New York, N.Y.)*, 324(2009), pp.759–764.

Knill, D.C. & Pouget, A., 2004. The Bayesian brain: The role of uncertainty in neural coding and computation. *Trends in Neurosciences*, 27(12), pp.712–719.

Kraus, B.J. et al., 2015. During Running in Place, Grid Cells Integrate Elapsed Time and Distance Run. *Neuron*, 88(3), pp.578–589.

Krupic, J. et al., 2015. Grid cell symmetry is shaped by environmental geometry. *Nature*, 518(7538), pp.232–235.

Kubie, J.L. & Fenton, A. a., 2012. Linear Look-Ahead in Conjunctive Cells: An Entorhinal Mechanism for Vector-Based Navigation. *Frontiers in Neural Circuits*, 6(April), pp.1–15.

Kunz, L. et al., 2015. Reduced grid-cell-like representations in adults at genetic risk for Alzheimer's disease. *Science*, 350(6259), pp.430–433.

Manjón, J. V et al., 2010. Adaptive non-local means denoising of MR images with spatially varying noise levels. *Journal of magnetic resonance imaging : JMRI*, 31(1), pp.192–203.

Mathis, A., Herz, A.V.M. & Stemmler, M., 2012. Optimal Population Codes for Space: Grid Cells Outperform Place Cells. *Neural Computation*, 24(9), pp.2280–2317.

Mathis, A., Herz, A.V.M. & Stemmler, M.B., 2013. Multiscale codes in the nervous system: The problem of noise correlations and the ambiguity of periodic scales. *Physical Review E - Statistical, Nonlinear, and Soft Matter Physics*, 88(2), pp.1–10.

McNaughton, B.L. et al., 2006. Path integration and the neural basis of the "cognitive map". *Nature reviews. Neuroscience*, 7(8), pp.663–78.

Moser, E.I. et al., 2014. Grid cells and cortical representation. *Nature Reviews Neuroscience*, pp.1–16.

Navarro Schröder, T. et al., 2015. Functional topography of the human entorhinal cortex. *eLife*, 4(JUNE), pp.1–17.

Navratilova, Z. et al., 2012. Phase precession and variable spatial scaling in a periodic attractor map model of medial entorhinal grid cells with realistic after-spike dynamics. *Hippocampus*, 22(4), pp.772–789.

O'Keefe, J. & Dostrovsky, J., 1971. The hippocampus as a spatial map. Preliminary evidence from unit activity in the freely-moving rat. *Brain Research*, 34(1), pp.171–175.

Poser, B.A. et al., 2010. Three dimensional echo-planar imaging at 7 Tesla. *NeuroImage*, 51(1), pp.261–6.

Pouget, A. et al., 2013. Probabilistic brains: knowns and unknowns. *Nature neuroscience*, 16(9), pp.1170–8.

Power, J.D. et al., 2012. Spurious but systematic correlations in functional connectivity MRI networks arise from subject motion. *NeuroImage*, 59(3), pp.2142–54.

Raudies, F. & Hasselmo, M.E., 2015. Differences in Visual-Spatial Input May Underlie Different Compression Properties of Firing Fields for Grid Cell Modules in Medial Entorhinal Cortex. *PLOS Computational Biology*, 11(11), p.e1004596.

Sreenivasan, S. & Fiete, I., 2011. Grid cells generate an analog error-correcting code for singularly precise neural computation. *Nature Neuroscience*, 14(10), pp.1330–1337.

Stemmler, M.B., Mathis, A. & Herz, A., 2015. Connecting Multiple Spatial Scales to Decode the Population Activity of Grid Cells. *Science Advances*, pp.1–12.

Stensola, H. et al., 2012. The entorhinal grid map is discretized. *Nature*, 492, pp.72–8.

Stensola, T. et al., 2015. Shearing-induced asymmetry in entorhinal grid cells. *Nature*, 518(7538), pp.207–212.

Taube, J.S., 2007. The head direction signal: origins and sensory-motor integration. *Annual review of neuroscience*, 30, pp.181–207.

Towse, B.W. et al., 2014. Optimal configurations of spatial scale for grid cell firing under noise and uncertainty. *Philosophical transactions of the Royal Society of London. Series B, Biological sciences*, 369(1635), p.20130290.

United States Department of the Army, 1996. Tactics, techniques, and procedures for field artillery survey.

Wilber, A.A. et al., 2014. Interaction of Egocentric and World-Centered Reference Frames in the Rat Posterior Parietal Cortex. *Journal of Neuroscience*, 34(16), pp.5431–5446.

Wolbers, T. et al., 2007. Differential recruitment of the hippocampus, medial prefrontal cortex, and the human motion complex during path integration in humans. *The Journal of neuroscience : the official journal of the Society for Neuroscience*, 27(35), pp.9408–16.

Yoshida, W. & Ishii, S., 2006. Resolution of Uncertainty in Prefrontal Cortex. *Neuron*, 50(5), pp.781–789.